ACS central science

http://pubs.acs.org/journal/acscii

Research Article

Durable Surfaces from Film-Forming Silver Assemblies for Long-Term Zero Bacterial Adhesion without Toxicity

Hossein Yazdani-Ahmadabadi, Demian F. Felix, Kai Yu, Han H. Yeh, Haiming D. Luo, Sara Khoddami, Lily E. Takeuchi, Amal Alzahrani, Srinivas Abbina, Yan Mei, Ladan Fazli, Dana Grecov, Dirk Lange,* and Jayachandran N. Kizhakkedathu*

Cite This: *ACS Cent. Sci.* 2022, 8, 546–561

Read Online

ACCESS | Metrics & More | Article Recommendations | Supporting Information

ABSTRACT: The long-term prevention of biofilm formation on the surface of indwelling medical devices remains a challenge. Silver has been reutilized in recent years for combating biofilm formation due to its indisputable bactericidal potency; however, the toxicity, low stability, and short-term activity of the current silver coatings have limited their use. Here, we report the development of silver-based film-forming antibacterial engineered (SAFE) assemblies for the generation of durable lubricous antibiofilm surface long-term activity without silver toxicity that was applicable to diverse materials via a highly scalable dip/spray/solution-skinning process. The SAFE coating was obtained through a large-scale screening, resulting in effective incorporation of silver nanoparticles (~10 nm) into a stable nonsticky coating with high surface hierarchy and coverage, which guaranteed sustained silver release. The lead coating showed zero bacterial adhesion over a 1 month experiment in the presence of a high load of diverse bacteria, including difficult-to-kill and stone-forming strains. The SAFE coating showed high biocompatibility and excellent antibiofilm activity *in vivo*.

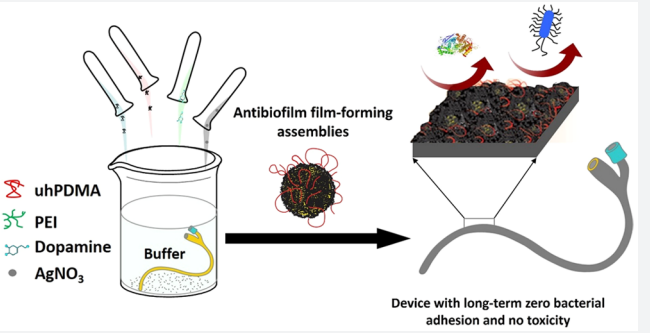

INTRODUCTION

Given that the surface of commercially available indwelling medical devices is highly prone to bacterial colonization and biofilm formation, their implantation into the body is disposed to a high risk of infection.[1−3] A potentially effective solution for preventing such infections is to treat the surface with robust antibiofilm coatings. Current antibiofilm coating technologies, including antifouling coatings,[4,5] contact-killing surfaces,[6−8] and antibiotic/bactericide releasing coatings,[9−13] have failed to endow long-term prevention of bacterial attachment and biofilm formation (>7 days).[14−16] The only coating with long-term null bacterial adhesion and high mechanical durability found in the literature was developed by Wang et al.[16] To achieve such a coating, they fabricated a zwitterionic hydrogel followed by bonding it to a flat surface with a commercially available cyanoacrylate glue. Despite its excellent mechanical robustness and long-term prevention of bacterial adhesion, major limitations for its use in medical devices are the poor film-forming capability and complicated coating fabrication.

One of the extensively used antimicrobial agents to generate release-killing coatings is silver, which possesses a strong bactericidal potency, has improved protection against microbial resistance, and can be prepared from economical precursors.[17−21] The most widely attempted approaches for the generation of silver release coatings include impregnation/postmodification of materials with silver and codeposition of silver on the surface.[22] The main limitations of the impregnation/postmodification methods include a compromised mechanical/dimensional stability of devices following impregnation, the use of environmentally unfriendly solvents such as chloroform, the highly limited silver release from deeply buried silver nanoparticles/clusters, fouling of the impregnated surface/superficially bound silver by proteins and bacteria with time, the substrate dependence of the coating process, and short-lived bactericidal activity.[23−26] An alternative attempt to address these issues is to codeposit silver with other coating materials.[27−29] The codeposition approach provides some benefits, including the use of a coating structure for silver deposition and prevention of a direct contact between silver and bacteria, which reduces surface fouling and cell toxicity. Despite these advances, the current codeposition solutions have failed to address the main issues, including the

Received: December 19, 2021
Published: April 27, 2022

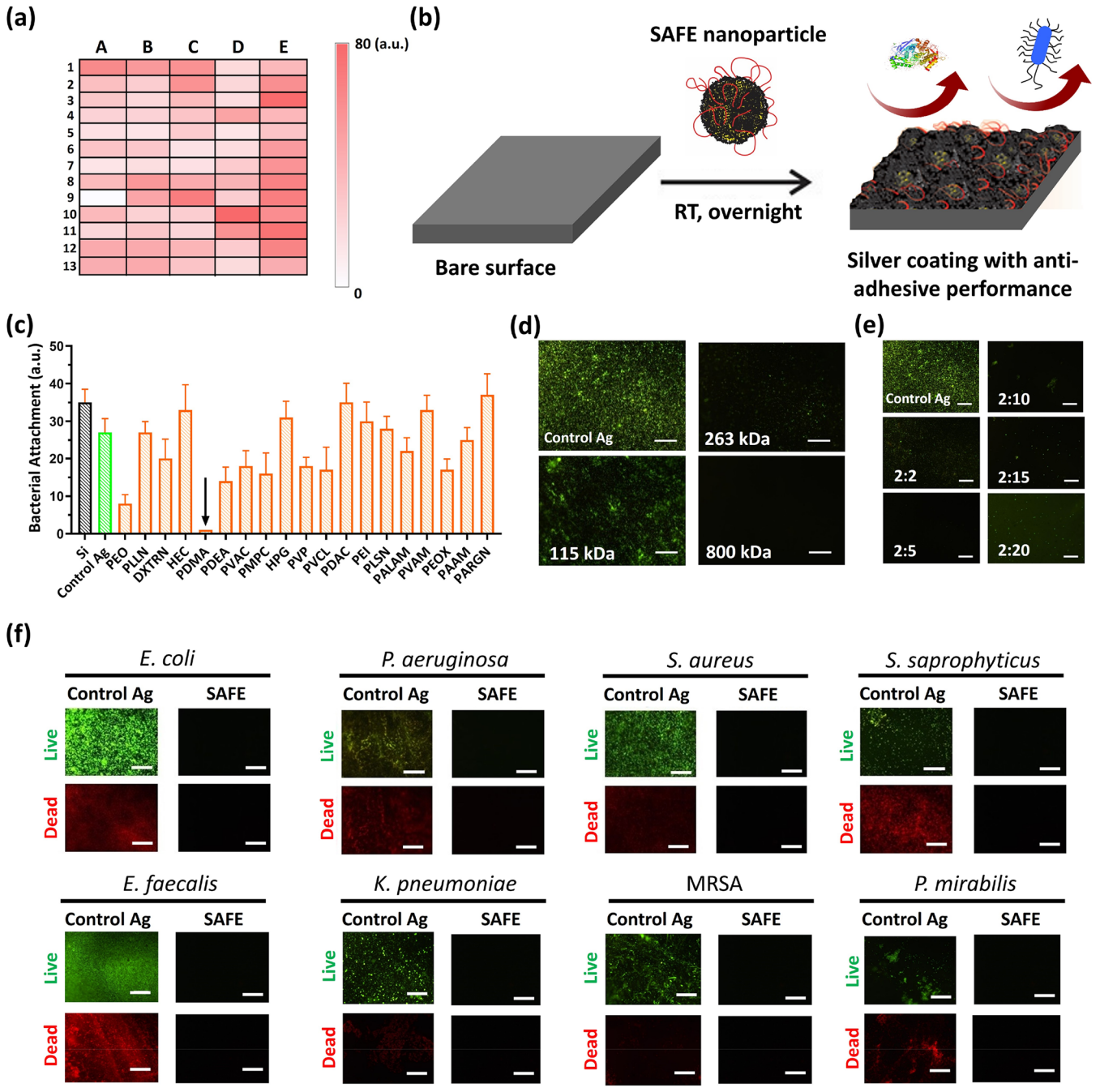

Figure 1. High-throughput screening and identification of SAFE composition. (a) Heat map of the high-throughput screening results from the bacterial adhesion assay (*E. coli*, initial concentration of 1×10^6 CFU/mL in LB, 24 h) (see also Table S1 for coating compositions corresponding to the heat map units). The color intensity indicates the bacterial load attached to the surface (white, no bacteria; intense red, high bacterial load). (b) Cartoon showing the synthesis of the SAFE coating with antiadhesive performance via a one-step dip-coating protocol at room temperature. (c) Relative bacterial attachment to the surface of coatings based on different UAPs incubated with *E. coli* (initial concentration of 1×10^6 CFU/mL in LB) for 7 days. The black downward arrow is used to highlight the excellent bacterial adhesion prevention of the PDMA-containing coating. (d) Fluorescence images of biofilm formation by *E. coli* (initial concentration of 1×10^6 CFU/mL in LB, 7 days) on the surface of coatings formed on the basis of different molecular weights of PDMA. (e) Fluorescence images of biofilm formation by *E. coli* (initial concentration of 1×10^6 CFU/mL in LB, 7 days) on the surface of coatings formed on the basis of different DA:PDMA mass ratios. (f) Fluorescence images (green, live bacteria; red, dead bacteria) showing biofilm formation on the surface of the "control Ag" coating and the SAFE coating after 4 weeks of coincubation with diverse bacterial strains (initail concentration: 1×10^6 CFU/mL). The scale bar is 100 μm.

uncontrolled release of silver, silver toxicity, surface fouling, short-lived activity, and a cumbersome coating synthesis.

Silver toxicity is the main subject in the debate over current silver coating technologies. To generate biocompatible silver release coatings, there are three main factors that should be avoided. These include uncontrolled release of silver ions, leaching of silver nanoparticles, and direct contact between silver nanoparticles and host cells.[30] It has been reported that eukaryotic cells are more resistant to silver toxicity in comparison with prokaryotic cells (e.g., bacterial cells), which

https://doi.org/10.1021/acscentsci.1c01556
ACS Cent. Sci. 2022, 8, 546−561

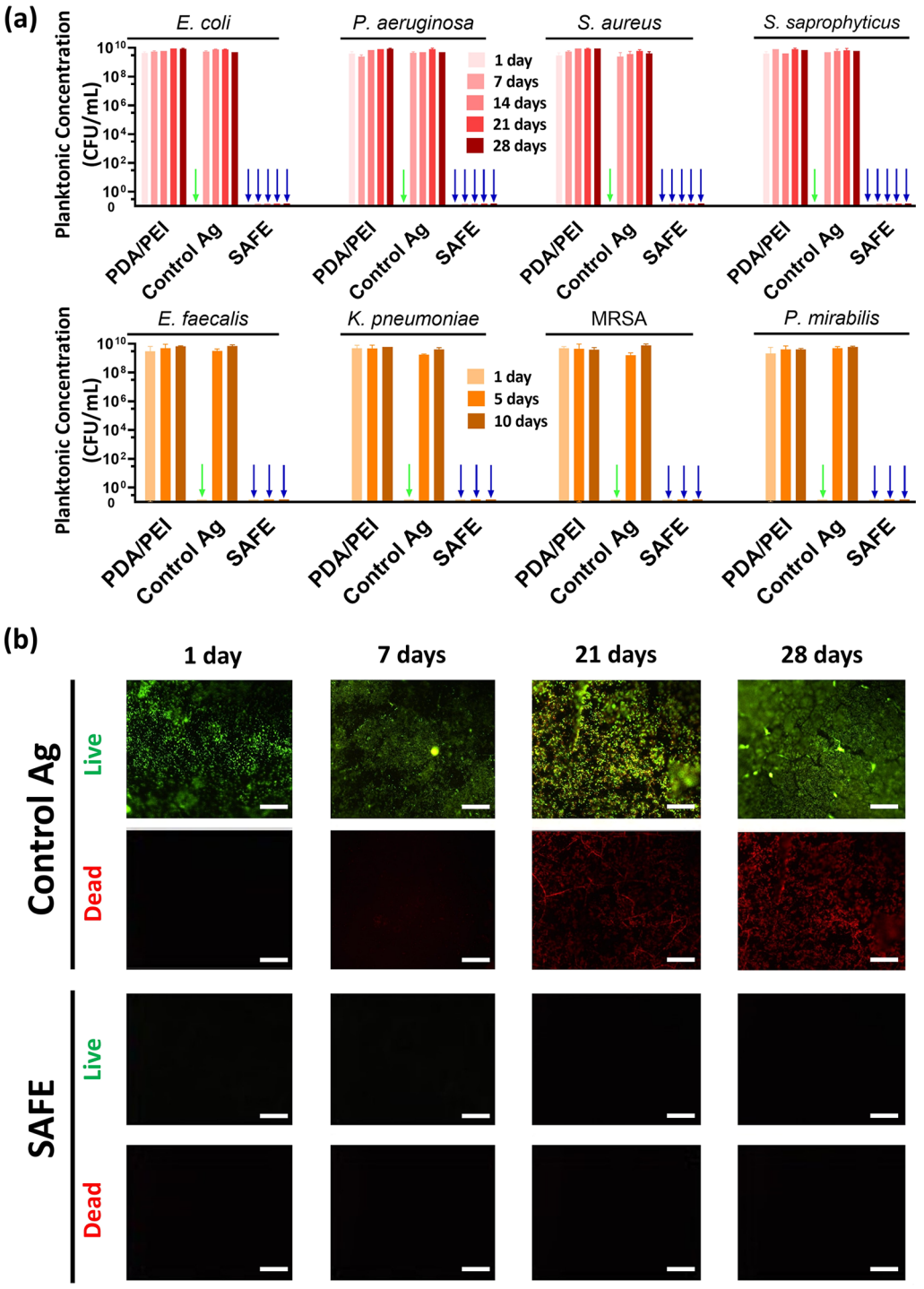

Figure 2. Long-term antibacterial activity of the SAFE coating. (a) Concentration of the planktonic bacteria present in the LB medium after coincubation of the coated polyurethane (PU) substrates (two controls including the PDA/PEI control and the "control Ag" coating along with the SAFE coating) with diverse bacterial strains (initial concentration of 1×10^6 CFU/mL in LB). The PDA/PEI control composition contains DA (2 mg/mL) and PEI (1.5 mg/mL). The downward arrows are used to highlight the prevention of planktonic bacterial growth (green, "control Ag"; blue, SAFE). (b) Fluorescence images (green, live bacteria; red, dead bacteria) showing the biofilm formation on the surface of the "control Ag" and the SAFE coating on PU substrates exposed to a stream of *S. saprophyticus* fluid (>1×10^9 CFU/mL, LB, 5 mL/min) for 28 days. The scale bar is 100 μm.

are highly susceptible to silver at significantly low concentrations (ppb level).[17,19,31] This difference in toxicity might be utilized for the generation of antibacterial surfaces based on silver that are nontoxic to host cells. To achieve controlled silver release, both the physical characteristics (thickness, surface coverage, and porosity) and nature of the silver (size, shape, and oxidation state) within the coating require consideration.[32] The development of a silver coating technology that encompasses all key factors, including controlled release, nontoxicity, simple coating synthesis, high durability, long-term activity, and high adaptability to diverse materials/devices, remains unmet.

https://doi.org/10.1021/acscentsci.1c01556
ACS Cent. Sci. 2022, 8, 546−561

In this work, we developed silver-based film-forming antibacterial engineered (SAFE) assemblies that form silver coatings with long-term null bacterial adhesion (>30 days) without silver toxicity, demonstrated both *in vitro* and *in vivo*. SAFE assemblies resulted in a lubricious surface coating with sustained long-term silver release, excellent surface coverage, and high mechanical durability on diverse surfaces and medical devices via a highly adaptable one-step dipping, spraying, or "solution-skinning" coating process.

RESULTS AND DISCUSSION

To develop the SAFE coating, we utilized a combination of two different molecular weight hydrophilic polymers (a low molecular weight amine containing polymer (LAP) and an ultrahigh molecular weight antifouling polymer (UAP)) with silver nitrate and a catecholamine. Our choice of the components stems from the current knowledge about catechol chemistry as a robust tool to design diverse functional coatings in combination with polyamines, the reduction of silver salts to nanoparticles in the presence of catechol derivatives, and the interaction of hydrophilic polymers with catecholamine polymers such as polydopamine (PDA).[33−38] To address the cumbersome synthesis of the current silver coatings, we developed an all-in-one coating composition that coats surfaces via a one-step process. The lead candidates were identified by utilizing two semi-high-throughput screenings.

Identification of SAFE Composition. We began with identification of the three-component system containing a LAP, a catecholamine, and a metal salt followed by a second screening to select the best UAP for the optimal four-component SAFE composition. We assessed the physical characteristics (wettability and thickness), bacterial killing activity and antiadhesion performance (over 24 h incubation with *E. coli*) of the coated surface (e.g., silicon wafer) with diverse three-component compositions (65 different combinations tested initially: Table S1) via a one-step dip-coating protocol at room temperature (Figures S1−S3). The characteristics we studied during this initial screening process were (1) generation of a relatively thick coating that can embed sufficient amount of silver for long-term sustained release and (2) a lower water contact angle of the coated surface, as it correlates with a high surface roughness and porosity of the coating. The anticipation was that a higher surface roughness and porosity of the coating would result in a larger accessible area for silver dissolution. The lowest water contact angle and the highest thickness were achieved for the coating with dopamine (DA) (2 mg/mL), silver nitrate (0.5 mg/mL), and low-molecular-weight PEI (PEI) (0.7 kDa, 1.5 mg/mL). This composition is named as "control Ag". We also tested different molecular weights of PEI (0.7, 10, and 25 kDa) in the generation of "control Ag" composition. We observed that the "control Ag" composition containing the medium (10 kDa)- or high-molecular-weight (25 kDa) PEI failed to generate a thick coating, possibly due to the steric stabilization of particles by this hydrophilic polymer, which leads to a poor particle deposition on the surface. The antiadhesion activity of surfaces treated with diverse coating combinations is represented as a heat map (Figure 1a). Among the diverse three-component compositions tested, the highest antiadhesion activity was observed for the "control Ag" coating (the unit A9 of the table shown in Figure 1a).

Despite the high antibacterial activity of the "control Ag" coating in the early stage (~24 h) (Figure S4a-i; there was no bacteria adhered on the surface for 24 h), it failed to prevent bacterial colonization of the surface for >7 days (Figure S4a-ii−v; the bacterial counts on the surface increased with time). To address this issue, we took advantage of specific interactions of UAPs with PDA. Diverse UAPs were tested in combination with the three-component "control Ag" to identify a composition that provided the long-term prevention of bacterial attachment (Figure 1b). We evaluated the antiadhesion property of surfaces treated with diverse four-component combinations (DA, PEI, silver nitrate, and a UAP) against *E. coli* (1×10^6 CFU/mL, 7 days) using a fluorescence microscopy technique. Among the UAPs tested, the highest antiadhesion activity was observed for poly(*N*,*N*-dimethylacrylamide) (PDMA) with ultrahigh molecular weight ($M_n \approx 1$ MDa) (Figure 1c,d and Figure S4b). In addition, the optimal DA:PDMA mass ratio was found to be 2:5 (Figure 1e). We label this composition the SAFE composition.

Next, we investigated the long-term antiadhesion performance of the SAFE coating against eight different bacterial species over 28 days. Unlike the "control Ag" coating, the SAFE coating completely suppressed bacterial attachment over 28 days irrespective of the bacterial species tested (Figure 1f and Figures S5 and S6). The lack of any bacteria (live or dead) on the SAFE coating indicates that it works via a unique mechanism, unlike previously attempted silver coatings that rely on contact killing or silver ion release, which result in the accumulation of dead bacteria or debris on the surface.[39,40]

To further clarify the important roles of each component of the SAFE composition in the complete inhibition of bacterial attachment and biofilm formation on the SAFE coating, we compared its antiadhesion property with that of two control coatings formed in the absence of silver (PDA/PEI/PDMA) and in the absence of PEI (DA/Ag/PDMA) utilizing fluorescence microscopy. The results showed that although the controls decreased the biomass deposition in comparison to the binary control coating with PDA/PEI, the surfaces were partially covered with live bacteria (Figure S7) demonstrating the importance of the presence of all four components for achieving the highest antibiofilm activity.

Long-Term Activity of SAFE Coating. Having identified the lead SAFE composition, we next investigated its broad-spectrum bacteria-killing activity. As expected, the PDA/PEI control did not show any bacteria-killing activity as it lacks silver, while the SAFE coating completely killed all planktonic bacteria over the 28 day experimental period irrespective of the bacterial strain tested (Figure 2a). In contrast, the "control Ag" coating inhibited the planktonic growth for only <7 days. We further investigated the long-term activity of the SAFE coating under challenging experimental conditions in which the coated surface was exposed to bacterial concentrations of $>1 \times 10^9$ CFU/mL with daily replenishment with fresh bacterial culture (*S. aureus*) over a 21-day period. Unlike the "control Ag" coating, which was covered by a thick biofilm, the SAFE coating showed no biomass accumulation during this period (Figure S8a). We further utilized a flow model previously developed in our laboratory,[35,41] as the flow (shear forces) is known to increase bacterial adhesion, colonization, and biofilm formation by some bacterial species (e.g., *E. coli* and *S. saprophyticus*). Under these conditions, the SAFE coating was found to completely inhibit bacterial biomass deposition by both Gram-negative (*E. coli*) and Gram-positive (*S. saprophyticus*) species in comparison to control samples, demonstrating its excellent long-term activity (Figure 2b, Figure S8b,c).

https://doi.org/10.1021/acscentsci.1c01556
ACS Cent. Sci. 2022, 8, 546−561

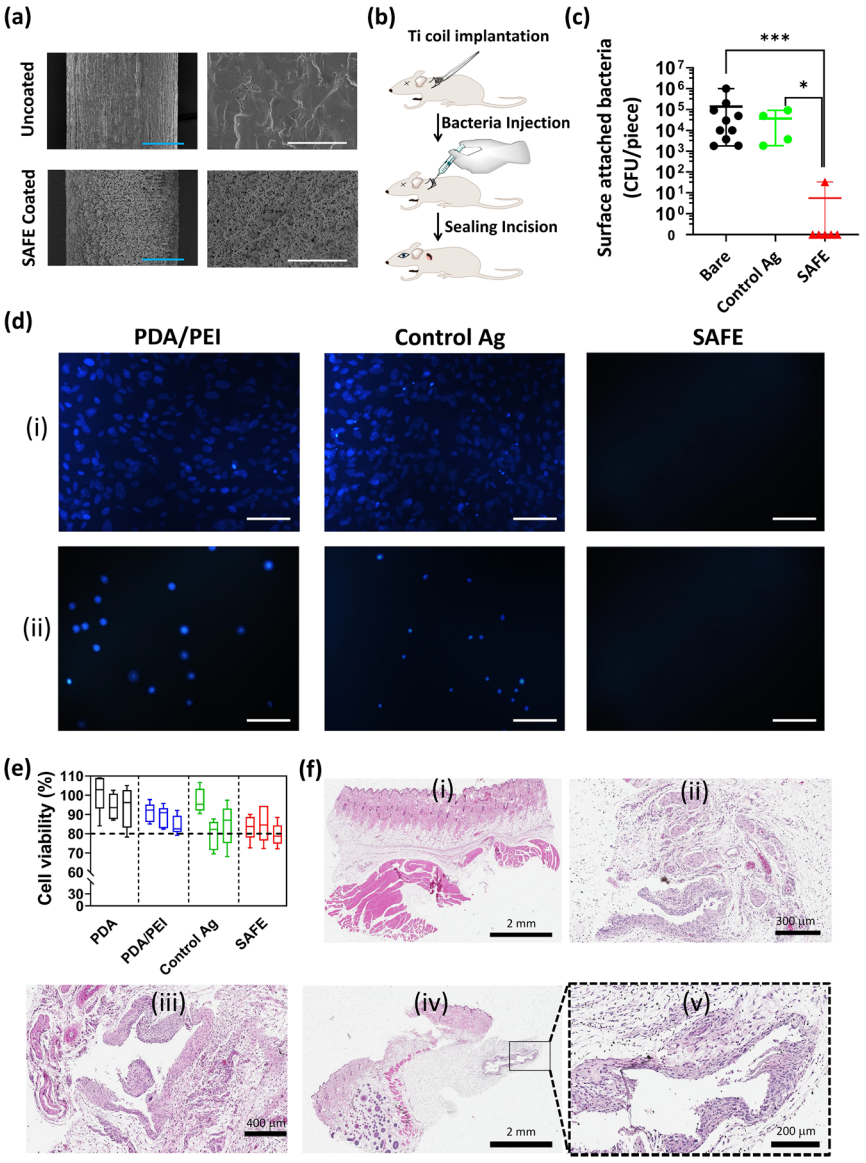

Figure 3. *In vivo* activity and biocompatibility of SAFE coating. (a) SEM images of the uncoated Ti wire and the SAFE-coated Ti wire at two different magnifications including 0.35 k (left) and 5 k (right). The blue and white scale bars are 100 and 10 μm, respectively. (b) Cartoon showing the insertion of the Ti implant under the skin on the back of the rat in the subcutaneous pocket. (c) Number of bacterial colonies attached to the surface of uncoated (n = 9), "control Ag" (n = 4), and SAFE coated (n = 6) Ti implants after 7 days of implantation in the subcutaneous pockets of rats. * indicates a P value ≤0.05, ** indicates a P value ≤0.01, and *** indicates a P value ≤0.001. (d) Fluorescence microscopy images of cell adhesion on the surface of the "control Ag" coating and the SAFE coating following 24 h incubation with (i) fibroblast and (ii) bladder cells (T24) at 37 °C. (e) Viability (%) of cells (T24 bladder cells) grown for 24 h in the media (RPMI, 10% FBS, 1% penicillin/streptomycin) incubated with different coatings, including PDA, PDA/PEI, "control Ag" and SAFE coatings (n = 5) at 12 h (left box), 24 h (middle box), and 48 h (right box). (f) Optical microscopy images of the H&E-stained section of (i) healthy skin tissue and skin tissues in vicinity of the (ii) uncoated Ti implant, (iii) "control Ag"-coated Ti implant, and (iv, v) SAFE-coated Ti implant.

***In Vivo* Efficacy of SAFE Coating in a Rat Infection Model.** Next, we investigated the efficacy of the SAFE coating in a rat subcutaneous infection model. A titanium (Ti) implant (Ti wire) treated with the "control Ag" coating or the SAFE coating was rolled in a coil and used for this experiment. The scanning electron microscopy (SEM) measurements confirmed the full coverage of the Ti surface with the SAFE coating (Figure 3a). Prior to the animal implantation, the prevention of bacterial adhesion of the SAFE-coated Ti coil was verified *in vitro* (*P. aeruginosa*, LB, initial concentration 1×10^7 CFU/mL, 7 days). The samples were implanted into subcutaneous pockets on the back of the animals followed by instilling of the pockets with *P. aeruginosa* prior to suturing the implantation site (Figure 3b). Animals recovered for 7 days, at which point the implants were removed and the bacterial attachment was assessed. The SAFE coating significantly reduced the number of bacteria on the implant in comparison to the uncoated and "control Ag"-coated samples. Except for one implant, all of the SAFE-coated implants showed zero bacterial counts on the surface. Overall, >4-log reduction in bacterial attachment was seen for the SAFE coated samples (Figure 3c).

***In Vitro* Cell/Protein Adhesion and *In Vivo* Biocompatibility of SAFE.** Having determined the activity of the SAFE coating *in vitro* and *in vivo*, the next step was to investigate its biocompatibility. The biocompatibility was assessed via cell viability and cell adhesion assays using

https://doi.org/10.1021/acscentsci.1c01556
ACS Cent. Sci. 2022, 8, 546−561

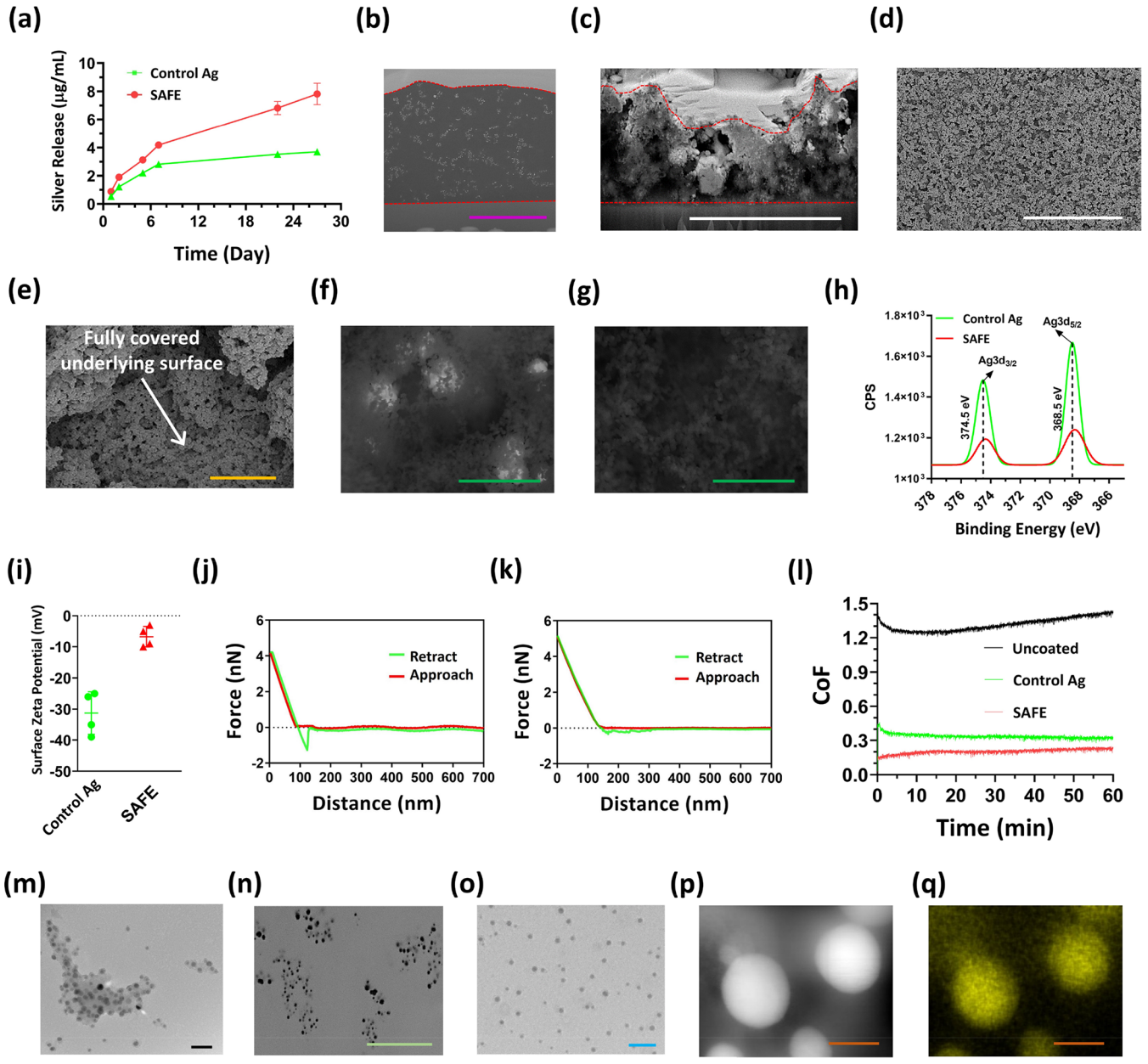

Figure 4. SAFE characterization. (a) Silver release profile for the "control Ag" coating and the SAFE coating over 28 days of incubation with water. SEM images of the FIB-created cross-section of (b) epoxy-embedded and (c) dehydrated SAFE coating on the silicon wafer. The purple and white scale bars are 4 and 5 μm, respectively. SEM images of the SAFE coating taken at two different magnifications: (d) 2 k and (e) 50 k. The yellow and white scale bars are 1 and 30 μm, respectively. The white arrow points out the full coverage of the underlying surface with the SAFE coating. BSE-SEM images of the (f) "control Ag" coating and (g) SAFE coating. The green scale bar is 400 nm. (h) High-resolution XPS spectra of silver for the "control Ag" coating and the SAFE coating. (i) Surface ζ potential of the "control Ag" coating (n = 4) and the SAFE coating (n = 4). Atomic force microscopy force−distance curves of (j) the "control Ag" coating and (k) the SAFE coating. (l) CoF of the coated glass against the PDMS ball (5 mm, 2 N) under wet conditions (water was used as the lubricant). The experiment was repeated three times, and the data presented are the average of the data collected from all three explements (n = 3). (m) TEM image of the solution-borne SAFE assemblies embedded with silver. The black scale bar is 30 nm. (n) Bright-field SEM image of the FIB-created cross section of the epoxy-embedded SAFE coating on a silicon wafer. The green scale bar is 400 nm. (o) TEM image of the reconstituted SAFE assemblies. The blue scale bar is 50 nm. (p) STEM dark field image and (q) silver mapping of the individual silver nanoparticle incorporated into the SAFE assembly/coating. The orange scale bar is 10 nm.

human fibroblasts (BJ) and urinary bladder cells (T24). We found that the SAFE coating effectively suppressed cell adhesion in comparison to the control coatings, which were covered with cells irrespective of the cell type tested (Figure 3d). The excellent cell-repelling property of the SAFE coating could be attributed to the presence of the antifouling PDMA.

Given the dose-dependent cytotoxicity of silver ions reported in the literature,[42−44] we further evaluated the tolerance of the SAFE coating *in vitro* and *in vivo*. Given the excellent cell-repelling property of the SAFE coating as discussed earlier, we were not able to directly evaluate the toxicity by standard cell-culture techniques using adherent cell lines. Thus, we assessed the toxicity of the supernatant of the SAFE coating that contains silver ions released from the coating. To that end, coated PU coupons (5 × 5 mm) were incubated in cell culture media (RPMI, 10% FBS, 1% penicillin/streptomycin) for

https://doi.org/10.1021/acscentsci.1c01556
ACS Cent. Sci. 2022, 8, 546−561

different time periods (12 and 24 h) and the collected supernatant was used for cell growth (T24 bladder cells). Since the amount of silver released (~0.3 μg/mL over 24 h (see the next section)) was higher than the MIC value of silver ions (<0.1 μg/mL),[45,46] the time period selected would provide representative data on the cell toxicity of the SAFE coating. Both silver-free (PDA and PDA/PEI controls) and silver-containing coating ("control Ag" and SAFE) groups showed high cell viability (>80%), suggesting that the coating is biocompatible (Figure 3e).

We further assessed the biocompatibility of the SAFE coating *in vivo*. To that end, we utilized a rat subcutaneous implantation model described earlier without the inclusion of bacteria. After a 7 day implantation period, tissues around the implants were excised and histologically evaluated for signs of toxicity in a blind fashion by a certified pathologist. The optical microscopy images of the stained tissue sections are shown in Figure 3f. Overall, there were no significant differences in the tissue response to either the "control Ag" coating or the SAFE coating. Immune cell infiltration and tissue damage were similar to those of the control Ti coils. No signs of toxicity were observed due to the release of silver ions into the tissue, suggesting that the amount of silver ions released by the SAFE coating is well-tolerated. Mild inflammatory infiltrates in the dermis and hypodermis were present for all groups, including tissues around uncoated implants, and were likely indicative of the normal healing process following the surgical procedure. In addition, a few specimens showed mild inflammatory reactions typical for a foreign body type reaction, which is expected given the fact that a Ti coil was implanted. The fact that no adverse effects suggestive of tissue toxicity upon implantation of the SAFE-coated implant demonstrate that the SAFE coating is biocompatible, consistent with our *in vitro* observations.

We further assessed the resistance of the SAFE coating against protein fouling. For this purpose, we utilized two different fluorescently labeled proteins, including fluorescein isothiocyanate tagged bovine serum albumin (FITC-BSA; 1 mg/mL, 1 h, 37 °C) and Alexafluor488-tagged fibrinogen (0.25 mg/mL, 1 h, 37 °C). The results are shown in Figure S9. To obtain quantitative data, the fluorescence images of protein adsorption were processed using the ImageJ platform. The results showed that the SAFE coating decreases FITC-BSA- and Alexafluor488-tagged fibrinogen deposition by >90% and 99%, respectively.

Sustained Silver Release, Thickness, and Surface Characterization of SAFE Coating. In order to understand the origin of the properties of the SAFE coating, we used the following measurements. We utilized inductively coupled plasma-optical emission spectroscopy (ICP-OES) to determine the amount of silver ions released from the coatings over 28 days. Unlike the "control Ag" coating, the SAFE coating showed a sustained silver release profile demonstrating ~8 μg/mL of silver released from the SAFE coating over 28 days, which is in the therapeutic range (Figure 4a and Figure S10a). The SAFE coating released silver ions and not silver nanoparticles, as was evident from the UV−vis spectra of the supernatant (Figure S10b).[47] The absence of absorption peaks in the near-visible region (400−450 nm) in the UV−vis spectrum of the deionized water incubated with the SAFE coating demonstrates that there were no silver nanoparticles released into the solution, which could be an asset for the coating, as silver nanoparticles are more susceptible to microbial resistance in comparison to silver ions.[48,49]

The release of silver ions from SAFE coatings prepared at different coating times (4, 12, 24, 48, and 72 h) (Figure S10c) showed that the silver release increased with the coating time, reaching ~2.6, 6.1, and 8 μg/mL for coatings formed after 4, 12, and 24 h coating times, respectively. However, for coating times longer than 24 h, the amount of silver ions released from the coating remained almost similar to that of the 24 h time point. The total amounts of silver incorporated into the "control Ag" coating and the SAFE coating were determined to be ~12 and 18 μg/mL, respectively (Figure S10d). Additionally, the average amount of silver ions released from the SAFE coating per day was ~0.3 μg/mL, which is much lower than the concentration reported in the literature that showed silver toxicity,[50,51] supporting the excellent tolerance of the SAFE coating demonstrated *in vitro* and *in vivo*. The size of silver nanoparticles within the SAFE coating decreased with time on immersion in water (28 days), indicating a considerable dissolution of silver nanoclusters (Figure S11a,b). The silver ion release was also affected by the DA:PDMA mass ratio, the optimal being 2:5, which was used in the SAFE coating (Figure S11c).

Next, we determined the wet and dry thicknesses of the SAFE coating utilizing the focused ion beam-scanning electron microscopy (FIB-SEM) technique.[52] To prepare samples for the wet thickness measurements, a SAFE-coated silicon wafer was embedded with an epoxy composition to prevent SAFE shrinkage during dehydration. The wet thickness of the SAFE coating was ~6 μm (Figure 4b). The structured organization of silver nanoparticles throughout the SAFE coating was clearly observed (this will be discussed further below). We also showed that the SAFE coating has a dry thickness of ~3.6 ± 0.5 μm, while the "control Ag" coating was found to be ~5 ± 1.8 μm thick (Figure 4c and Figure S12a). The significant difference in the dry and wet thicknesses of the SAFE coating demonstrated the structural reorganization of the SAFE coating from a loose structure under wet conditions to a dense structure following dehydration.

We further used SEM to analyze the surface morphology of the SAFE coating. The SAFE coating showed a hierarchical structure with high surface roughness and full surface coverage (Figure 4d,e). The SAFE coating was less porous in comparison to the "control Ag" coating, which resembles nanofibrillar scaffolds (Figure S12b). We also utilized back-scattered electron mode SEM (BSE-SEM) to evaluate the chemical heterogeneity of the SAFE surface. Superficial silver aggregates with a size of 300−400 nm were observed on the "control Ag" coating (Figure 4f), while the surface of the SAFE coating was found to be chemically homogeneous and clear of superficial silver aggregation, which might have reduced the cell toxicity and fouling of the surface caused by the direct contact between cells/proteins and silver clusters (Figure 4g).

The surface composition of the SAFE coating was determined using an X-ray photoelectron spectroscopy (XPS) analysis. The disappearance of the Si peak of the SAFE spectrum supports the full surface coverage of the silicon wafer with the SAFE coating (Figure S13a and Table S2). The effective incorporation of silver was indicated by the characteristic peak at ~375 eV corresponding to the Ag 3d (Figure 4h). The attenuation of the silver peak for the SAFE coating confirmed the enrichment of nonsilver materials (PDA, PEI, and PDMA) on the silver assembly, which is consistent with BSE-SEM observations discussed previously (Figure 4h). The nitrogen (N 1s)/carbon (C 1s) ratio was used as a measure of

https://doi.org/10.1021/acscentsci.1c01556
ACS Cent. Sci. 2022, 8, 546−561

surface enrichment of the SAFE coating with PDMA. The N/C ratios were found to be 0.18 and 0.28 for the "control Ag" coating and the SAFE coating, respectively (Table S2). Among the three organic components of the SAFE composition (DA, PEI, and PDMA), the highest and lowest theoretical N/C ratios belong to PEI (0.5) and DA (0.125), respectively. The N/C ratio calculations showed an increase in value with the use of PDMA, suggesting the partial replacement of PDA with either PDMA or PEI on the surface of the SAFE coating.

The C 1s XPS spectra were deconvoluted into three peaks at 284.1, 285.3, and 287.1 eV, which were assigned to C−OH, C−N, and C−C, respectively (Figure S13b−d). The C−C/C−N peak intensity ratio of the SAFE spectrum was higher than that of the "control Ag" spectrum, demonstrating the presence of PDMA on the surface. The N 1s XPS spectra of the controls (PDA coating and "control Ag" coating) were fitted to three peaks (398.4, 399.5, and 400.5 eV, which correspond to =N−C, C−N−C, and N−C, respectively) (Figure S13e,f). However, the N 1s XPS spectrum of the SAFE coating included two peaks at 399.5 and 401.5 eV, which could be attributed to C−N−C and N−C= O, respectively, demonstrating the presence of the PDMA amide group (Figure S13g). The O 1s XPS data confirmed the presence of both hydroxyl and quinone on the surface of all three coatings (Figure S13h−j). The O 1s spectrum of the SAFE coating showed an additional peak at 532.8 eV, which could be attributed to C= O of PDMA. Overall, the XPS data confirmed the incorporation of PDMA onto the surface of the SAFE coating.

To further probe the PDMA incorporation, we employed surface ζ potential and atomic force microscopy (AFM) measurements under wet conditions. Unlike the "control Ag", the surface ζ potential of the SAFE coating exhibited a near-neutral surface charge (∼−5 mV) (Figure 4i), which indicates that the negative charge of PDA was shielded by neutral PDMA chains. The AFM approach curve of the SAFE coating showed a typical steric profile offered by a surface-anchored hydrophilic polymer on a surface (Figure 4j,k).[53] The retraction curves suggested the formation of a looplike assembly of hydrophilic polymer chains on the surface of the SAFE coating, while such features were not observed for the "control Ag" coating. The wettability of the SAFE coating was measured using water contact angle measurements. The SAFE coating showed a very low water contact angle of <10° (Figure S14) possibly due to the presence of highly hydrophilic PDMA and high surface roughness with the hierarchical nanoparticle assembly.[54] In comparison, the PDA control coating is hydrophilic with a water contact angle value of ∼50° and the "control Ag" coating has a water contact angle of <10° (Figure S14).

Mechanical Stability and Lubricity of SAFE Coating. We also evaluated the lubricity/abrasion resistance of the SAFE coating utilizing a tribometric analysis. The coefficient of friction (CoF) of the SAFE coating was ∼0.1, which was lower than those of the "control Ag" coating (∼0.3) and the uncoated substrate (glass) (∼1.4), demonstrating the high lubricity of the SAFE surface (Figure 4l). The significantly lower CoF of the SAFE surface is due to the presence of the looplike assembly of PDMA on its surface. Additionally, it was shown that there is no change in the CoF of the SAFE coating during the tribometry measurements (1 h), which indicates that the SAFE coating possesses high abrasion resistance.

We further tested the mechanical stability of the SAFE coating under other test conditions, including exposing the SAFE coating to sonication in water for 10 min, rubbing the SAFE surface with a piece of tissue paper 30 times back and forth, immersing the SAFE coating in an aqueous solution containing 70 vol % ethanol for 24 h, and sterilizing the SAFE coating by autoclaving at 120 °C and 15 psi for 1 h. The surface morphology of the SAFE coating that underwent mechanical challenges was nearly the same as that of the original SAFE coating (Figure S15a−d). Although the roughness of the SAFE surface decreased upon rubout, the surface retained its structure and full surface coverage (Supporting Movies 1−3). The surface of the coated substrate retained its original appearance with no detectable attachment upon 30 back and forth rubs (Figure S15e). The surface of the tissue paper rubbed over (30 back and forth rubs) the SAFE-sprayed glass did not show any stain or detectable materials released, demonstrating the high robustness of the SAFE coating (Figure S15f). As shown in Figure S16, there was no difference between the antiadhesion performance of the exposed SAFE coating and that of the as-made SAFE coating.

Evidence for Formation of Assemblies and Deposition in SAFE Coating Process. Our hypothesis was that the *in situ* formation and deposition of stabilized silver-based assemblies are responsible for the remarkable performance of the SAFE coating. To probe this, we characterized the formation of assemblies in a SAFE solution. A broad absorbance over the visible region was observed for both the "control Ag" and SAFE suspensions, suggesting that the introduction of PDMA into a DA solution did not significantly affect DA oxidation reactions (Figure S17a). The high absorbance across the whole spectral region confirms the *in situ* formation of silver nanoparticles.[55−57] The average hydrodynamic size of SAFE assemblies was ∼100 nm (the distribution profile is shown in Figure S17b; size range 80−200 nm), however, the average particle size of the "control Ag" aggregates was around 350 nm with a much broader distribution of sizes (200−800 nm). This is consistent with the BSE-SEM size measurement of superficially formed silver aggregates of the "control Ag" coating (discussed earlier). Further, the ζ potential of SAFE assemblies was ∼5 mV, which is much lower than that of "control Ag" aggregates (∼25 mV) (Figure S17c). Together, these data suggested that the *in situ* formed SAFE assemblies are highly stabilized and the neutral PDMA provides good shielding of surface negative charges on the nanoparticles/assemblies.

A TEM analysis of the solution-borne SAFE assemblies revealed the presence of well-dispersed 10 nm nanoparticles containing a silver core (Figure 4m and Figure S17d). The SAFE solution showed assemblies (∼100 nm) containing small silver nanoparticles (∼10 nm) embedded. However, large silver aggregates were observed for the "control Ag" coating (Figure S17e), supporting the BSE-SEM observations for the "control Ag" coating. The digital images showed that the SAFE coating solution is more stable than the "control Ag" and the PDA control solutions (Figure S17f). The SAFE solution was very stable for >60 days without precipitation, while the "control Ag" solution showed aggregates, indicating the lack of long-term stability. The increased stability of the SAFE suspension could be attributed to the stabilizing effect of PDMA.[29]

Next, we assessed the organization of silver nanoparticles within the SAFE coating following deposition by focused-ion beam-high resolution scanning electron microscopy (FIB-HRSEM). The results showed that the SAFE coating was loaded with nanoparticles as large assemblies (Figure 4n), which is consistent with the TEM images of the solution-borne

https://doi.org/10.1021/acscentsci.1c01556
ACS Cent. Sci. 2022, 8, 546−561

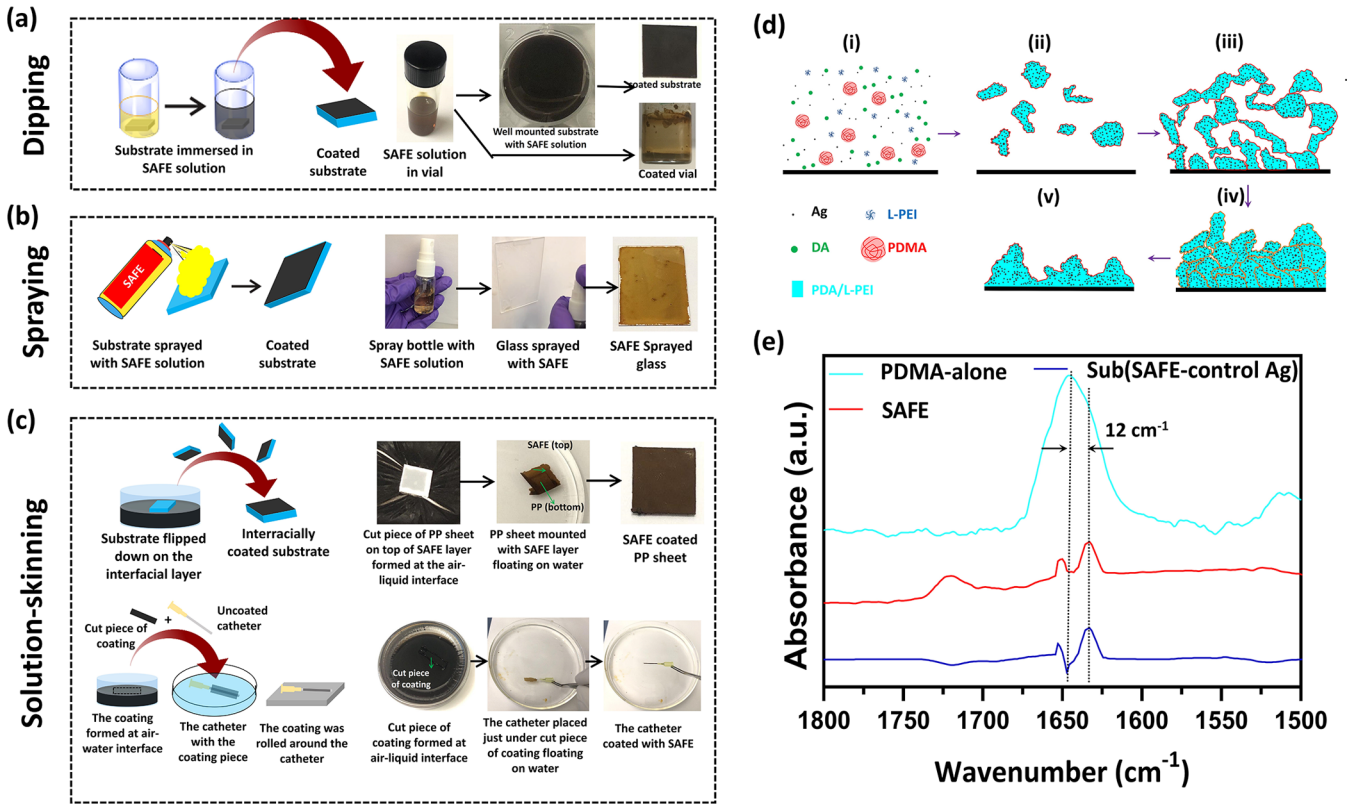

Figure 5. SAFE film formation. Schematic along with digital images showing different coating methods including (a) dipping, (b) spraying, and (c) solution-skinning. (d) Schematic shows different steps of the SAFE film formation based on the mechanism we proposed utilizing the SAFE assemblies and coating characterization: (i) a substrate exposed to a solution containing DA, PEI, silver nitrate, and PDMA at $t = 0$; (ii) the formation of irregularly shaped assemblies embedded with silver nanoparticles; (iii) the random deposition of assemblies forming a structurally loose film; (iv) reorganization of the film structure upon dehydration; (v) formation of the reorganized assemblies with a highly integrated and dense structure. (e) ATR-FTIR spectrum of the SAFE coating, spectrum of PDMA alone, and the spectrum resulting from the subtraction of SAFE spectrum from "control Ag" spectrum, denoted Sub (SAFE − "control Ag").

SAFE assemblies. Overall, the solution-borne SAFE assemblies retained their structural organization during film formation. The TEM results showed that the size of individual silver nanoparticles incorporated into the SAFE coating was ∼10 nm (Figure 4o), which is in agreement with the electron microscopy data discussed earlier. The elemental mapping measurements confirmed that the small nanoparticles incorporated into the SAFE assemblies/coating are silver (Figure 4p,q). The sustained silver release of the SAFE coating (discussed earlier) can be attributed to the high surface area provided by the incorporation of such small nanoparticles (∼10 nm) into a thick, highly hydrated, nonsticky coating with high surface hierarchy.

Adaptability of SAFE Coating Composition for Different Coating Processes. We further illustrated the versatility of the SAFE coating to dipping, spraying, and solution-skinning processes. To dip-coat the surface, the substrate was immersed in the SAFE solution overnight under static conditions (Figure 5a). Diverse materials/devices (e.g., Ti wire, polypropylene (PP) surgical mesh, bandage, and gauze) were effectively coated using the dip-coating process (Figure S18). The water contact angle of all surfaces coated was <10°, indicating the successful formation of the SAFE coating (Figure S18). Dip-coated surfaces were used for analyses and studies described in the previous sections. Further, the SAFE composition was also found to be sprayable (Figure 5b and Supporting Movie 4), resulting in a uniform coating (Figure 5b, the last image on the right). The solution-skinning process refers to the formation of a coating layer at the interface of the coating solution and air. We took advantage of the oxygen-dependent formation of polydopamine to generate a freestanding film at the air−water interface.[58] The solution-skinning film was successfully transferred to diverse materials and polymeric catheters with different sizes and chemistries (Figure 5c and Supporting Movies 5 and 6). Collectively, the data showed that diverse materials or medical devices can be effectively coated with the SAFE composition via different coating methods, demonstrating the versatility of the SAFE-coating process (Figure S19). Since we noticed some changes in the thickness of the coatings prepared by different methods, we anticipate that it may affect their long-term activity. However, this needs to be evaluated further.

Mechanism of SAFE Film Formation. On the basis of the characterization data discussed earlier and that available in the literature,[35,41] we proposed a mechanism for the formation of the SAFE coating as shown in Figure 5d. In the initial stage, silver nanoparticles were formed *in situ* upon mixing all four components (DA, PEI, silver nitrate, and PDMA), aided by the oxidation of DA. The assembly of such silver nanoparticles (∼10 nm) with time led to the formation of silver assemblies (∼100 nm) containing PDA, PEI and PDMA (Figure 5d-i,ii). The silver assemblies retained their stability due to the presence of PEI and PDMA, which provided electrostatic and steric stabilization, respectively. The resulting silver assemblies

https://doi.org/10.1021/acscentsci.1c01556
ACS Cent. Sci. 2022, 8, 546−561

slowly adsorbed on the surface without sedimentation, providing a loose structural organization (Figure 5d-iii). Upon dehydration, the structured assemblies were reorganized and resulted in a dense structure with high stability (Figure 5d-iv,v). The strong interactions (electrostatic interactions and covalent bonding) between PEI and PDA[5,59,60] in conjunction with the filler effect of silver could be the main reasons for the high stability of the coating.[61,62] PDMA reorganized on the surface to provide nonsticky characteristics of the SAFE coating.

Next, we utilized attenuated total reflectance-Fourier transform infrared (ATR-FTIR) spectroscopy to probe the PDA−PDMA interactions within the SAFE coating (Figure 5e). There is a red shift of ∼12 cm^{-1} for the peak corresponding to the carbonyl of PDMA within the SAFE coating (1621 cm^{-1}) in comparison to that of the PDMA-alone control (1633 cm^{-1}). This red shift demonstrated the hydrogen bonding between the carbonyl groups of PDMA and the hydrogen donors of PDA (hydroxyl and amino groups) that is responsible for the stabilization of PDMA within the SAFE coating. The data are consistent with previous reports on PDA−PDMA interactions.[35,41] With this, we proposed a molecular architecture for the SAFE structure (Figure S20). The main intermolecular interactions involved in the SAFE formation include the hydrogen bonds of the carbonyl group of PDMA with PDA hydrogen donors (hydroxyls and amines), covalent bonds formed between PDA and PEI via Michael-type addition reactions, and coordinate bonds between silver and PDA/PEI.[63] We also utilized SEM to evaluate the morphology of the SAFE coating formed at different time points (15 min and 2, 8, 12, 24, 48, and 72 h) (Figure S21). The morphology of the SAFE coatings formed within coating times of longer than 24 h (48 and 72 h) remained unchanged, demonstrating that the SAFE film formation is relatively fast (<24 h time needed to reach the full surface coverage) and self-limiting. However, none of these data and analyses conclusively support the covalent bond formation between PEI and PDA at this time. Since many of the peaks from different components and their reaction products are overlapping, the current methods did not provide evidence for a covalent structure. Additional analyses are needed to address this.

CONCLUSIONS

In summary, we reported the development of a nontoxic durable silver-based coating from SAFE assemblies via a simple dip/spray/solution-skinning coating process resulting in long-term zero bacterial adhesion. The coating composition was identified through a library screening approach with four different components providing surface binding, stability, antiadhesion, and antimicrobial properties. Detailed surface analyses provide mechanistic information regarding the formation of nanostructures, the self-assembly process, film formation, and the coating stabilization. We demonstrated that the sustained release of silver ions at therapeutic doses in combination with the excellent antiadhesion property of the coating resulted in zero bacterial adhesion and colonization for several weeks. The coating showed broad-spectrum antibiofilm activity, was able to prevent infection in a rat infection model, and was found to be highly biocompatible *in vitro* and *in vivo* without silver toxicity. The current coating is anticipated to have broad application for diverse medical devices and implants to prevent implant-/device-associated infections.

EXPERIMENTAL SECTION

Materials. All catechol reagents, including dopamine (DA) hydrochloride, serotonin (Ser) hydrochloride, pyrogallol (PG), 2,3,5-benzenetriol (BTO), tannic acid (TA), pyrocatechol (PC), and resorcinol (Res), and all metal salts, including silver nitrate, gallium nitrate, zinc nitrate, copper(II) nitrate, nickel(II) nitrate, and gold(III) chloride were purchased from Sigma-Aldrich and used as received. Low-molecular-weight polyethylenimine (700 Da), gentamicin, poly(vinyl amine) (PVAM, 6 kDa), methylcellulose, and crystal violet were also purchased from Sigma-Aldrich. 4-arm-PEG-NH_2 (2 kDa) was purchased from Advanced BioChemicals. A number of hydrophilic polymers used in this work, including poly(ethylene oxide) (PEO; 1000 kDa), polyacrylamide (PAAM; 400 kDa), dextran (DXTRN; 500 kDa), poly(2-ethyl-2-oxazoline) (PEOX; 500 kDa), polyvinylpyrrolidone (PVP; 1300 kDa), poly diallyl ammonium chloride (PDAC; 400 kDa), polyethylenimine (PEI; 700 kDa), poly(L-lysine) (PLSN; 150 kDa), and polyarginine (PARGN; 70 kDa), were supplied by Sigma-Aldrich. Poly(*N*,*N*-diethylacrylamide) (PDEA; 1040 kDa), poly(*N*-vinyl caprolactam) (PVCL; 354 kDa), and poly(*N*-vinylamine) (PVAM; 120 kDa) were purchased from Polymer Source, and polyallylamine (PALAM) hydrochloride (150 kDa), pullulan (PLLN,) and 2-hydroxyethyl cellulose (HEC; 1000 kDa) were purchased from Polysciences Inc. Poly(*N*,*N*-dimethylacrylamide) with different molecular weights (MWs)/polydispersity indices (PDIs) (medium-molecular-weight PDMA, MW = 150 kDa/PDI = 1.32; high-molecular-weight PDMA, MW = 260 kDa/PDI = 1.5; ultrahigh-molecular-weight PDMA, MW = 1 MDa, PDI = 1.4) was synthesized on the basis of a previously reported procedure from our group.[35] Diverse biomedical plastic materials, including polyethylene (PE), polypropylene (PP), polystyrene (PS), polydimethylsiloxane (PDMS), polyvinyl chloride (PVC), polycarbonate (PC), polyethylene terephthalate glycol (PTEG), and polyurethane (PU), stainless steel (SS), a silicon wafer (Si), and titanium (Ti), were obtained from Professional Plastics (USA). The catheters (Bardex, 24G PU IV, 10 Fr silicone urinary, and 16 Fr PVC urinary catheter) were purchased from BD Company. Titanium (Ti) wire (diameter 25 mm) was purchased from Thermo-Fisher Scientific. All cell-culture-related media and supplements (Trypsin-EDTA, Dulbecco's phosphate-buffered saline (DPBS), heat-inactivated fetal bovine serum (FBS), penicillin/streptomycin (P/S), and Roswell Park Memorial Institute (RPMI) 1640 medium) were obtained from Life Technologies Inc. unless specified otherwise. Human BJ fibroblasts were purchased from Cedarlane Corporation (Burlington, Ontario). T24 bladder carcinoma cells were purchased from the American Type Culture Collection (ATCC CRL-2922 Manassas, VA). Modified Eagle's medium (MEM) was purchased from Gibco. Methanol was purchased from Fisher Scientific. SYLGARD 184 was purchased from Dow Corning (Midland, MI, US). An MTS assay (CellTiter 96 AQueous One Solution Cell Proliferation Assay, catalogue #G3582) was purchased from Promega.

Methods. *Control PDA/PEI Coating Synthesis.* To prepare the PDA/PEI control coating, LMW-PEI (1.5 mg/mL) was dissolved in Tris buffer solution (10 mM, pH 8.5). DA (2 mg/mL) was added to the resulting solution. The two-component solution was vortexed for 30 s to prepare the PDA suspension. Then, the PDA suspension (500 μL) was transferred to wells

https://doi.org/10.1021/acscentsci.1c01556
ACS Cent. Sci. 2022, 8, 546−561

(48-well plate) containing the working substrate. The well plate was covered with Parafilm to prevent the water loss upon the coating process. After 24 h, the substrate was removed, washed gently with deionized water, and dried in air.

Control PDA/L-PEI/PDMA Coating. To prepare the coating, PDMA (5 mg/mL) was dissolved in Tris buffer solution (10 mM, pH 8.5). L-PEI (1.5 m/mL) and DA (2 mg/mL) were added to the PDMA solution and mixed on a vortexer for 30 s. Then, the resulting suspension was transferred to wells containing the working substrate and kept for 24 h at room temperature with a Parafilm cover on top. Finally, the substrate was removed, washed gently with deionized water, and dried in air.

Control PDA/Ag/PDMA Coating. To prepare the coating, PDMA (5 mg/mL) was dissolved in Tris buffer solution (10 mM, pH 8.5). DA (2 mg/mL) and silver nitrate (0.5 mg/mL) were added to the PDMA solution and mixed on a vortexer for 30 s. Then, the resulting suspension was transferred to a well containing the working substrate and kept for 24 h at room temperature with a Parafilm cover on top. Finally, the substrate was removed, washed gently with deionized water, and dried in air.

"Control Ag" Coating Synthesis. To prepare the "control Ag" coating, L-PEI (1.5 mg/mL) and silver nitrate (0.5 mg/mL) were dissolved in Tris buffer solution (10 mM, pH 8.5). DA (2 mg/mL) was added to the resulting solution. The three-component solution was vortexed for 30 s to prepare the suspension. Then, the suspension (500 μL) was transferred to wells (48-well plate) containing the working substrate. The well plate was covered with Parafilm to prevent water loss upon the coating process. After 24 h, the substrate was removed, washed gently with deionized water, and dried in air.

SAFE Coating Synthesis. To prepare the dipping SAFE coating, PDMA (5 mg/mL) was dissolved in Tris buffer solution (10 mM, pH 8.5). L-PEI (1.5 mg/mL), silver nitrate (0.5 mg/mL), and DA (2 mg/mL) were added to the PDMA solution and mixed on a vortexer for 30 s. Then, the resulting suspension was transferred to wells containing the working substrate and kept for 24 h at room temperature with a Parafilm cover on top. Finally, the substrate was removed, washed gently with deionized water, and dried in air. To prepare coatings based on different DA:PDMA ratios (2:2, 2:10, 2:15, and 2:20), different concentrations of PDMA (2, 10, 15, and 20 mg mL^{-1}, respectively) were prepared in Tris buffer solution, as opposed to 5 mg/mL. To prepare coatings based on other hydrophilic polymers, the same coating procedure as for the SAFE coating was used except that the PDMA was replaced with other hydrophilic polymers. To prepare the sprayable SAFE coating, the substrate was sprayed using the same solution used for the dipping SAFE fabrication. The thickness and stability of the sprayed SAFE coating was adjusted using the volume of solution sprayed. The sprayed substrate was left on the benchtop overnight to fully dry. To coat flat substrates with the SAFE composition via the solution-skinning method, the substate was faced down on the surface of the SAFE coating layer formed at the interface of air and the SAFE solution. After 10 min, the substrate was removed and flipped down so that the coated side was facing upward. The coated substrate was left on the benchtop overnight to fully dry. To coat cylindrical substates, i.e., catheters, the coating formed at the interface of air and the SAFE solution was floated on water. Then, the catheter was placed underneath the coating layer floating on water and was removed with the coating bound to the surface. The coated catheter was left in air overnight to fully dry. To coat PDMS balls, the needle-supported PDMS balls (diameter: 5 mm) were just placed on top of the coating formed at the water−air interface in wells (48-well plate, 1 mL suspension, overnight) and gently pushed down until the coating was detached from the well wall. Then the needle-supported PDMS balls were moved down until the whole ball was submerged. Afterward, the coated PDMS balls were withdrawn and shaken in water for a few seconds to remove unbound materials followed by drying at room temperature.

Polymer Characterization. The molecular weight and polydispersity index (PDI) of PDMA were measured by GPC on a Waters 2690 separation module fitted with a DAWN EOS multiangle laser light scattering detector from Wyatt Technology Corp. with a refractive index detector (Optilab DSP from Wyatt Technology Corp.).

Water Contact Angle Measurements. Water contact angle measurements were utilized to analyze the wettability of the coated substrates. A water droplet (4 μL) was placed on the working substrate followed by taking the image of the droplet by using a digital camera (Retiga 1300, Q-imaging Co.) at five different spots. The value of the contact angle was obtained using Northern Eclipse software.

Scanning Electron Microscopy. A Helios scanning electron microscope (SEM; FIE, USA) with an accelerating voltage of 1 kV was used to analyze the coating morphology utilizing the secondary electron (SE) mode. To preserve the morphology of the wet coating, samples were dehydrated via an ethanol dehydration method including serial incubation of the working sample with different ethanol aqueous solutions (50, 60, 70, 80, 90, 95, and 100 vol %) for 10 min within each solution. Ethanol-dehydrated samples were placed in a critical point drying machine to dry samples in the presence of supercritical carbon dioxide. To prepare samples for SEM imaging, dried samples were attached on the SEM stub by double-sided carbon tape followed by mounting with a silver paint to prevent drifting issues while imaging. Then, all mounted samples were coated with a 10 nm iridium (Ir) layer by using a Leica sputter coater (working distance 3 cm and current 80 mA). A focused-ion beam (FIB) was also utilized to create cross sections to determine the wet/dry thicknesses by coupling with SEM. The FIB created cross section was imaged at the same time under SEM to measure the thickness of the coating layer on a silicon wafer. We also investigated the dispersion of silver nanoparticles and their size distribution inside the coating utilizing FIB-SEM measurements. We used a method recently reported.[52] Briefly, we initially treated samples with a two-component epoxy formulation (epoxy precursor and curing agent) to fill up the pores of the coating. Then, the epoxy-filled samples were cured at room temperature overnight. The ion beam was used to create a cross section for backscattered electron (BSE) imaging (working distance 4 mm, accelerating voltage 2 kV, current density 50 pA).

Transmission Electron Microscopy. Transmission electron microscopy (TEM) (FEI, USA) was employed to analyze the size of the silver nanoparticles incorporated into the coating and provide an elemental mapping analysis. To prepare TEM samples, the coatings were scraped off by a sharp razor blade from the Si wafer surface and transferred into a 1.5 mL microtube containing 1 mL of Tris buffer. Afterward the tube was placed in a bath sonicator to homogenize the particles. Then a droplet of the prepared suspension was placed on a TEM grid with an ultrathin carbon film on a lacey carbon

https://doi.org/10.1021/acscentsci.1c01556
ACS Cent. Sci. 2022, 8, 546−561

support film. The acceleration voltage used for the TEM analysis was adjusted to be 100 kV.

Atomic Force Microscopy Analysis. The force−distance measurements were carried out by using a multimode atomic force microscope with a maximum scan size of 130 × 130 μm^2. The measurements were performed with a Nanoscope IIIa controller (Digital Instruments, Santa Barbara, CA). A V-shaped cantilever made of silicon nitride in the front and gold layer in the back for the reflection of the laser beam (DNP-S10, Bruker) was utilized. The force−distance data were acquired by conducting the tip extension and the tip retraction in order. The rate of the tip movement was set up to be 0.5 mm/s for both the approach and retraction periods. The number of replications for each sample was 13. The rupture distance and adhesive force were measured.

X-ray Photoelectron Spectroscopy Analysis. X-ray photoelectron microscopy (XPS) was utilized to assess the incorporation of silver into the coating and the composition of coatings. An Omicron XPS instrument equipped with an EA125 energy analyzer and DAR400 Dual X-ray performing with an Mg Kα source was used. The XPS samples were prepared by coating silicon wafers with coating compositions.

Inductively Coupled Plasma-Optical Emission Spectroscopy. Coated PU samples (5 × 5 mm) were immersed in 1 mL of deionized water for 1 month. The 1 mL portion of water was removed at various intervals and replaced with another 1 mL portion of fresh deionized water. The collected supernatant portions were mixed with 2 mL of a 2 wt % nitric acid solution and subsequently used to measure the amount of silver ions released from coatings by using an ICP instrument equipped with a Varian 725ES optical emission spectrometer (OES). Also, in order to measure the total concentration of silver embedded in the coating, the coating was digested by using a nitric acid/hydrogen peroxide (1/1.5) mixture at 100 °C for 2 h. The resulting supernatant was diluted with deionized water to a total volume of 3 mL and used for ICP-OES analysis.

Dynamic Light Scattering Measurements. The ζ potential and hydrodynamic size of nanoparticles were measured using a Zetasizer instrument (Malvern). A 10 μL portion of a solution containing nanoparticles was added to 1 mL of filtered water. The diluted solution was transferred to a disposable cuvet for hydrodynamic size measurements. Then, the same solution was transferred to cuvets designed for ζ potential measurements. The surface ζ potential (SZP) extension of the instrument (Zetasizer, Malvern) was also used to analyze the ζ potential of the coating at the surface. The coated PU samples were mounted on the SZP probe and fit into a cuvet containing 1 mL of a ζ potential transfer standard suspension (DTS1235). The ζ potential of the system was measured at different places to extrapolate the ζ potential at the surface.

Ellipsometry Analysis. A variable-angle spectroscopic ellipsometer (VASE) (J.A. Woollam, Lincoln, NE) was employed to determine the thickness of thin coatings on silicon wafers utilizing the Cauchy model. The VASE spectra were obtained at different angles, including 55, 65, and 75°, in a range of 480−700 nm. The instrument was equipped with an M-2000 50W quartz tungsten halogen light source to illuminate the samples. WVASEE32 analysis software was employed to fit the data for a determination of the coating thickness.

Light Absorbance Measurements. UV−vis measurements were carried out using a multimode plate reader (Molecular Science) to obtain the absorbance spectra (200−500 nm) of different solutions.

Attenuated Total Reflectance Fourier Transform Infrared (ATR-FTIR). ATR-FTIR spectra of uncoated and coated PU sheets were collected on a Burker 670 TensoII instrument with an MCT/A liquid-nitrogen-cooled detector, a KBr beam splitter, and a VariGATR Grazing Angle accessory. Spectra were recorded at 2 cm^{-1} resolution, and 128 scans were collected.

Bacterial Culture. The antibacterial activity of diverse materials (5 × 5 mm squares)/devices (1 cm long pieces) treated with different coatings was analyzed by a planktonic growth assay. The uncoated and "control Ag"-coated materials/devices referred to the controls. Different bacterial strains were grown from freezer stocks and subcultured once prior to use in experiments. These included *P. aeruginosa*, *E. coli*, *S. aureus*, *S. saprophyticus*, *E. faecalis*, *K. pneumoniae*, methicillin-resistant *S. aureus* (MRSA) and *P. mirabilis*, at 37 °C. Starting concentrations of 1×10^6 and 1×10^8 CFU/mL were prepared from overnight subcultures in LB and used initial inoculations for flow and challenging conditions respectively. Both shaking and flow models were used to assess bacterial adhesion and biofilm formation on different surfaces.

Shaking Experiments (Nonchallenging and Challenging Conditions). The samples were sterilized by incubating them in a 48-well plate containing 1 mL of 70% ethanol solution for 5 min, followed by three washes in sterile LB. Once the the last washing step was completed, 500 μL of the subcultured bacterial solution was added to the same well containing the coated materials/devices. The samples were placed on a shaker at 100 rpm at 37 °C. Every 24 h, half of the medium was replaced with fresh bacteria (1×10^3 CFU/mL). Samples were removed at specified time intervals and analyzed for biofilm formation.

Flow Experiments (Challenging Conditions). The samples (5 × 5 mm PU pieces) were placed inside rubber tubes, sterilized via autoclaving prior to the experiment. The tubes were attached to a peristatic pump, and the flow rate was set at 5 mL/min. The ends of the tubes were placed in a 1 L Erlenmeyer flask containing 400 mL of a bacterial solution (initial concentration 1×10^9 CFU/mL). Every 24 h, half of the medium was replaced with fresh bacterial solution (1×10^9 CFU/mL). Samples were removed at specified time intervals and analyzed for biofilm formation.

Planktonic Bacterial Growth Analysis. To assess the number of planktonic bacteria in the surrounding medium of varying samples, a portion of the medium was removed and serially diluted in fresh LB. 10 μL of each dilution was spot plated on LB Agar plates in triplicate and incubated at 37 °C overnight. Visible colonies were counted to assess the number of planktonic bacteria. Portions of diluted solutions (10 μL) were placed on preset agar plates and stored at 37 °C overnight. Then, the planktonic colonies appearing on the plate were counted.

Bacterial Adhesion Analysis. Samples were removed from the bacterial culture at different times and rinsed five times with 1 mL of sterile PBS. Then, the samples were gently immersed in 500 μL of a fluorescent dye solution containing SYTO9 (3 μL/mL) and propidium iodide (3 μL/mL) dissolved in deionized water. After 20 min, the samples were removed and gently washed five times with 1 mL of sterile deionized water followed by a dehydration process through the same gradient ethanol method described earlier. Finally, the

https://doi.org/10.1021/acscentsci.1c01556
ACS Cent. Sci. 2022, 8, 546−561

dehydrated samples were observed under a fluorescence microscope (Zeiss Axioskop 2 plus, Carl Zeiss Microimaging Inc.). In some cases, bacterial adhesion was assessed utilizing SEM analysis. To prepare samples for SEM, the samples incubated with bacteria (*E. coli*) were taken out at different time points and washed five times with sterile PBS. The washed samples were gradually dehydrated using different ratios of ethanol to water, described earlier. The dehydrated samples were mounted on SEM stubs by double-sided carbon tape, and silver paint was used to prevent drifting issues upon electron microscopy imaging. The mounted samples were then coated with a 10 nm layer of iridium (Ir) to increase the sample conductivity.

To count the colonies attached to the surface of the samples, we utilized an agar-plate spotting method. The samples were removed, washed five times with sterile PBS, and then transferred to 1.5 mL microtubes containing 1 mL of sterile PBS. The tubes were placed in a sonication bath for 10 min. The supernatants were removed and serially diluted with sterile PBS. Portions of the diluted solutions (10 μL) were placed on preset agar plates and stored at 37 °C overnight. The percentage of bacterial reduction was calculated from the colony count.

Coating Stability Measurements. The abrasion resistance of the coating was assessed using a conventional T50 pin-on-disk tribometer (Nanovea, Irvine, CA, US). The friction coefficient was measured during the experiment. A constant disk rotation speed of 60 rpm was applied over a wear radius of 5 mm, and a constant weight of 2 N was applied normally to the pin. Polydimethylsiloxane (PDMS) tribo-pairs were used to mimic human soft tissue with water used as the lubricant for friction assessment. PDMS balls with a diameter of 6 mm were cast in a 3D-printed mold with a standard 10:1 mixing ratio. The PDMS-coated glass tribo-pair was cured at room temperature for 24 h followed by high-temperature curing at 100 °C for 35 min. This allowed the air bubbles trapped in the 3D-printed mold during the casting process to have sufficient time to surface. The PDMS tribo-pair then underwent an allylamine plasma treatment and coating after 24 h of resting at room temperature to change the hydrophobic surface into a hydrophilic surface. The coated samples were exposed to different testing conditions. Afterward, the exposed SAFE-coated samples were tested to evaluate their antiadhesion property against *E. coli* under nonchallenging conditions (initial concentration 1×10^6 CFU/mL). The surface morphology of the exposed coatings was also assessed using SEM and compared with those of the original coatings. The first stability test was performed by exposure of the sample to ultrasonication. To do this, a SAFE coated PP piece in a 1.5 mL microtube containing 1 mL of PBS was kept in the sonication bath for 10 min. To assess the rub resistance of the coating, a SAFE-coated PP piece was rubbed back and forth 30 times using a piece of paper towel. Then, the amount of detached coating was visualized. In the case of the sterilization test, a SAFE-coated PP piece was placed under autoclave conditions used for the sterilization of equipment/solids for 1 h or immersed in 70 vol % ethanol for 24 h.

Cell Adhesion Measurements. The cells were cultured in RPMI 1640 medium with 10% FBS and 1% P/S at 37 °C and 5% CO_2. When they reached 70% confluence, cells were dissociated with 0.25% trypsin and 0.05% EDTA (Gilco, 25300062), pelleted by centrifugation at 300*g*, and resuspended with complete RPMI-1640 medium. Tissue culture chamber slides (6-well, Falcon) were treated with the "control Ag" coating and SAFE coating. Cells were seeded at 30000 cells per well in coated chamber slides containing various coatings and allowed to settle for 24 h. Afterward, cells were washed three times with cold DPBS and fixed with 4% PFA for 15 min at ambient temperature. Fixed cells were stained with nuclear stain, Hoescht 33342 (1:10000 dilution; Thermofisher Scientific). Slides were mounted with Fluorimount-G mounting medium (SouthernBiotech Birmingham, AL). Cell adhesion was visualized using a Zeiss Axioscope 2 Plus fluorescent microscope.

MTS Assay. The samples (coatings on PU sheets 5 × 5 mm^2) were prepared as described previously. To assess the cytocompatibility, coatings were submerged in 70% ethanol for 5 min for sterilization and rinsed with PBS before adding them to 48-well plates. Then, RPMI mediun supplemented with 10% FBS and 1% penicillin/streptomycin was added to each well (1 mL). The samples were left with the medium for 12 and 24 h to allow release of silver ions. The collected media were then used to test for cytocompatibility on T24 cells that were cultured using RPMI media supplemented with 10% FBS and 1% penicillin/streptomycin up to passage 15 at 37 °C and 5% CO_2. When the cells reached 80−90% confluence, they were dissociated using trypsin and collected at 300*g*. The harvested T24 cells were cultured in 96-well plates at a seeding density of 1×10^5 cells/well. After the cells were allowed to adhere for 24 h, the old media were aspirated and cells were rinsed with PBS prior to adding the collected media from the coatings. The cells were left for 24 h prior to subjecting them to an MTS assay performed according to the supplier protocol to determine cell viability. Viability was assessed against control cells growing in fresh complete media.

Protein Adsorption Measurements. Fluorescence microscopy was utilized to assess the adsorption of two different proteins including fluorescein isothiocyanate tagged bovine serum albumin (FITC-BSA) and Alexafluor488-tagged fibrinogen onto the surface. The uncoated PP and SAFE-coated PP samples were incubated with the fluorescent-labeled protein solutions (1 mg/mL FITC-BSA and 0.25 mg/mL Alexafluor488-tagged fibrinogen at pH 7.4) for 1 h at 37 °C. Afterward, the samples were taken off and gently washed three times with PBS to remove unbound proteins. The washed samples were then visualized using a Zeiss Axioscope 2 Plus fluorescent microscope.

In Vivo Efficacy Studies. The animal experimental protocols were approved by the University of British Columbia Animal Care Committee. To determine the efficacy of our coating to prevent bacterial biofilm formation and subsequent infection in an *in vivo* setting, we utilized a subcutaneous implant infection model in rats. For this, an 8 mm incision was made on either side of the median line on the dorsal aspect of each animal. A subcutaneous pocket was formed by a blunt dissection technique large enough to insert a 1 cm × 0.5 cm titanium coil implant that was either coated or uncoated. Each animal received a SAFE-coated sample as well as a control. Infection was induced by the introduction of 1×10^8 *P. aeruginosa* CFU (per 50 μL of PBS) into the pocket. Following implantation, the incisions were closed with absorbable sutures in a subcuticular fashion and the animals were recovered for 7 days. On day 7, the animals were sacrificed, the implants were removed, and adherent bacteria were quantified using spot plating and CFU counts of serially diluted samples.

https://doi.org/10.1021/acscentsci.1c01556
ACS Cent. Sci. 2022, 8, 546−561

In Vivo Toxicity Studies. To assess the toxicity of coatings, a subcutaneous rat model was used. Briefly, an 8 mm incision was made on either side of the median line on the dorsal aspect of each animal. A subcutaneous pocket was formed by a blunt dissection technique large enough to insert a 1 cm × 0.5 cm titanium wire implant that was either coated or uncoated. Each animal received an uncoated, SAFE-coated and control-coated Ti implant. Following implantation, the incisions were closed with absorbable sutures in a subcuticular fashion and the animals were recovered for 7 days. On day 7, the animals were sacrificed and the tissue surrounding the implant was removed, fixed in buffered formalin, mounted in paraffin, sectioned, and stained using hematoxylin and eosin. The samples were visualized using an optical microscope (Zeiss Axioskop 2 plus, Carl Zeiss Microimaging Inc.).

Statistical Analysis. The average values ± standard deviation (SD) are reported. A two-sample unpaired *t* test method by Excel (Data/Data Analysis/Unequal variances) was used. A statistically significant value was set as $P < 0.05$.

■ ASSOCIATED CONTENT

Supporting Information

The Supporting Information is available free of charge at https://pubs.acs.org/doi/10.1021/acscentsci.1c01556.

Additional data, and figures and tables supporting our conclusions (lead candidate identification, SAFE coating development, SAFE surface characterization, SAFE assembly characterization, antibacterial studies, stability measurements, and SAFE versatility and antifouling experiments) (PDF)

Rubbing out process on glass coated with a SAFE coating (MP4)

Rubbing out process on a PP coupon coated with a SAFE coating (MP4)

Rubbing out process on a PU coupon coated with a SAFE coating (MP4)

Spray-coating process using a SAFE solution (MP4)

Skinning coating process on a PP coupon using the SAFE layer formed at the air−liquid interface (MP4)

Solution-skinning process on a PDMS ball using the SAFE layer formed at the air−liquid interface (MP4)

■ AUTHOR INFORMATION

Corresponding Authors

Jayachandran N. Kizhakkedathu − *Department of Chemistry, University of British Columbia, Vancouver, British Columbia V6T 1Z3, Canada; Centre for Blood Research, Life Science Institute, Department of Pathology and Laboratory Medicine, and The School of Biomedical Engineering, University of British Columbia, Vancouver, British Columbia V6T 1Z3, Canada;* orcid.org/0000-0001-7688-7574; Email: jay@pathology.ubc.ca

Dirk Lange − *The Stone Centre at Vancouver General Hospital, Department of Urologic Sciences, University of British Columbia, Vancouver, British Columbia V5Z 1M9, Canada*; Email: dlange@mail.ubc.ca

Authors

Hossein Yazdani-Ahmadabadi − *Department of Chemistry, University of British Columbia, Vancouver, British Columbia V6T 1Z3, Canada; Centre for Blood Research, Life Science Institute, University of British Columbia, Vancouver, British Columbia V6T 1Z3, Canada*

Demian F. Felix − *The Stone Centre at Vancouver General Hospital, Department of Urologic Sciences, University of British Columbia, Vancouver, British Columbia V5Z 1M9, Canada*

Kai Yu − *Centre for Blood Research, Life Science Institute and Department of Pathology and Laboratory Medicine, University of British Columbia, Vancouver, British Columbia V6T 1Z3, Canada*

Han H. Yeh − *Department of Mechanical Engineering, University of British Columbia, Vancouver, British Columbia V6T 1Z4, Canada*

Haiming D. Luo − *Department of Chemistry, University of British Columbia, Vancouver, British Columbia V6T 1Z3, Canada; Centre for Blood Research, Life Science Institute, University of British Columbia, Vancouver, British Columbia V6T 1Z3, Canada*

Sara Khoddami − *The Stone Centre at Vancouver General Hospital, Department of Urologic Sciences, University of British Columbia, Vancouver, British Columbia V5Z 1M9, Canada*

Lily E. Takeuchi − *Centre for Blood Research, Life Science Institute and Department of Pathology and Laboratory Medicine, University of British Columbia, Vancouver, British Columbia V6T 1Z3, Canada*

Amal Alzahrani − *The Stone Centre at Vancouver General Hospital, Department of Urologic Sciences, University of British Columbia, Vancouver, British Columbia V5Z 1M9, Canada*

Srinivas Abbina − *Centre for Blood Research, Life Science Institute, University of British Columbia, Vancouver, British Columbia V6T 1Z3, Canada*

Yan Mei − *Centre for Blood Research, Life Science Institute and Department of Pathology and Laboratory Medicine, University of British Columbia, Vancouver, British Columbia V6T 1Z3, Canada;* orcid.org/0000-0003-2500-0659

Ladan Fazli − *Vancouver Prostate Centre, Department of Urologic Sciences, University of British Columbia, Vancouver, British Columbia V6H 3Z6, Canada*

Dana Grecov − *Department of Mechanical Engineering, University of British Columbia, Vancouver, British Columbia V6T 1Z4, Canada; The School of Biomedical Engineering, University of British Columbia, Vancouver, British Columbia V6T 1Z3, Canada*

Complete contact information is available at: https://pubs.acs.org/10.1021/acscentsci.1c01556

Notes

The authors declare the following competing financial interest(s): The University of British Columbia has filed for patent protection on the technology described here. H.Y.-A., K.Y., D.L., and J.N.K. are named as inventors on a PCT patent application submitted. The rest of the authors declare no competing interests.

■ ACKNOWLEDGMENTS

The authors acknowledge funding by Canadian Institutes of Health Research (CIHR), the Natural Sciences and Engineering Council of Canada (NSERC), the Canada Foundation for Innovation (CFI), and the British Columbia Knowledge Development Fund. H.Y.-A., L.E.T., and H.D.L. acknowledge

NSERC NanoMat CREATE funding. L.E.T. and H.D.L. acknowledge NSERC CGS-M scholarships. J.N.K. holds a Career Investigator Scholar award from the Michael Smith Foundation for Health Research (MSFHR). S.A. acknowledges a MSFHR postdoctoral fellowship. We also acknowledge 4D LABORATORIES at Simon Frasor University (SFU) for providing TEM services and the Bioimaging facility and Center for High-throughput Phenogenomics (CHTP) at the University of British Columbia. All animal studies were approved by the University of British Columbia Animal Care Committee. Animal studies were performed at the Jack Bell Research Centre, Vancouver General Hospital (UBC animal ethics approval no. A17−0297). All data have been presented in the main text or in the Supporting Information.

REFERENCES

(1) Onaizi, S. A.; Leong, S. S. J. Tethering Antimicrobial Peptides: Current Status and Potential Challenges. *Biotechnol. Adv.* **2011**, *29* (1), 67−74.
(2) Raphel, J.; Holodniy, M.; Goodman, S. B.; Heilshorn, S. C. Multifunctional Coatings to Simultaneously Promote Osseointegration and Prevent Infection of Orthopaedic Implants. *Biomaterials* **2016**, *84*, 301−314.
(3) Yu, K.; Lo, J. C. Y.; Mei, Y.; Haney, E. F.; Siren, E.; Kalathottukaren, M. T.; Hancock, R. E. W.; Lange, D.; Kizhakkedathu, J. N. Toward Infection-Resistant Surfaces: Achieving High Antimicrobial Peptide Potency by Modulating the Functionality of Polymer Brush and Peptide. *ACS Appl. Mater. Interfaces* **2015**, *7* (51), 28591−28605.
(4) Yong, Y.; Qiao, M.; Chiu, A.; Fuchs, S.; Liu, Q.; Pardo, Y.; Worobo, R.; Liu, Z.; Ma, M. Conformal Hydrogel Coatings on Catheters to Reduce Biofouling. *Langmuir* **2019**, *35* (5), 1927−1934.
(5) Zhou, C.; Wu, Y.; Thappeta, K. R. V.; Subramanian, J. T. L.; Pranantyo, D.; Kang, E. T.; Duan, H.; Kline, K.; Chan-Park, M. B. In Vivo Anti-Biofilm and Anti-Bacterial Non-Leachable Coating Thermally Polymerized on Cylindrical Catheter. *ACS Appl. Mater. Interfaces* **2017**, *9* (41), 36269−36280.
(6) Watson, G. S.; Green, D. W.; Watson, J. A.; Zhou, Z.; Li, X.; Cheung, G. S. P.; Gellender, M. A Simple Model for Binding and Rupture of Bacterial Cells on Nanopillar Surfaces. *Adv. Mater. Interfaces* **2019**, *6* (10), 1801646.
(7) Pandit, S.; Cao, Z.; Mokkapati, V. R. S. S.; Celauro, E.; Yurgens, A.; Lovmar, M.; Westerlund, F.; Sun, J.; Mijakovic, I. Vertically Aligned Graphene Coating Is Bactericidal and Prevents the Formation of Bacterial Biofilms. *Adv. Mater. Interfaces* **2018**, *5*, 1701331.
(8) Yi, G.; Yuan, Y.; Li, X.; Zhang, Y. ZnO Nanopillar Coated Surfaces with Substrate-Dependent Superbactericidal Property. *Small* **2018**, *14*, 1703159.
(9) Hizal, F.; Zhuk, I.; Sukhishvili, S.; Busscher, H. J.; Van Der Mei, H. C.; Choi, C. H. Impact of 3D Hierarchical Nanostructures on the Antibacterial Efficacy of a Bacteria-Triggered Self-Defensive Antibiotic Coating. *ACS Appl. Mater. Interfaces* **2015**, *7* (36), 20304−20313.
(10) Sadrearhami, Z.; Shafiee, F. N.; Ho, K. K. K.; Kumar, N.; Krasowska, M.; Blencowe, A.; Wong, E. H. H.; Boyer, C. Antibiofilm Nitric Oxide-Releasing Polydopamine Coatings. *ACS Appl. Mater. Interfaces* **2019**, *11* (7), 7320−7329.
(11) Zhuk, I.; Jariwala, F.; Attygalle, A. B.; Wu, Y.; Libera, M. R.; Sukhishvili, S. A. Self-Defensive Layer-by-Layer Films with Bacteria-Triggered Antibiotic Release. *ACS Nano* **2014**, *8* (8), 7733−7745.
(12) Albright, V.; Zhuk, I.; Wang, Y.; Selin, V.; van de Belt-Gritter, B.; Busscher, H. J.; van der Mei, H. C.; Sukhishvili, S. A. Self-Defensive Antibiotic-Loaded Layer-by-Layer Coatings: Imaging of Localized Bacterial Acidification and PH-Triggering of Antibiotic Release. *Acta Biomater.* **2017**, *61*, 66−74.
(13) Pant, J.; Gao, J.; Goudie, M. J.; Hopkins, S. P.; Locklin, J.; Handa, H. A Multi-Defense Strategy: Enhancing Bactericidal Activity of a Medical Grade Polymer with a Nitric Oxide Donor and Surface-Immobilized Quaternary Ammonium Compound. *Acta Biomater.* **2017**, *58*, 421−431.
(14) Smith, R. S.; Zhang, Z.; Bouchard, M.; Li, J.; Lapp, H. S.; Brotske, G. R.; Lucchino, D. L.; Weaver, D.; Roth, L. A.; Coury, A.; et al. Vascular Catheters with a Nonleaching Poly-Sulfobetaine Surface Modification Reduce Thrombus Formation and Microbial Attachment. *Sci. Transl. Med.* **2012**, *4* (153), 132.
(15) Ahmadabadi, H. Y.; Yu, K.; Kizhakkedathu, J. N. Surface Modification Approaches for Prevention of Implant Associated Infections. *Colloids Surf., B* **2020**, *193*, 111116.
(16) Wang, W.; Lu, Y.; Zhu, H.; Cao, Z. Superdurable Coating Fabricated from a Double-Sided Tape with Long Term "Zero" Bacterial Adhesion. *Adv. Mater.* **2017**, *29* (34), 1606506.
(17) Panáček, D.; Hochvaldová, L.; Bakandritsos, A.; Malina, T.; Langer, M.; Belza, J.; Martincová, J.; Večeřová, R.; Lazar, P.; Poláková, K.; et al. Silver Covalently Bound to Cyanographene Overcomes Bacterial Resistance to Silver Nanoparticles and Antibiotics. *Adv. Sci.* **2021**, *8* (12), 2170065.
(18) Wong, K. K. Y.; Liu, X. Silver Nanoparticles - The Real "Silver Bullet" in Clinical Medicine? *Medchemcomm* **2010**, *1* (2), 125−131.
(19) Panáček, A.; Kvítek, L.; Smékalová, M.; Večeřová, R.; Kolář, M.; Röderová, M.; Dyčka, F.; Šebela, M.; Prucek, R.; Tomanec, O.; et al. Bacterial Resistance to Silver Nanoparticles and How to Overcome It. *Nat. Nanotechnol.* **2018**, *13* (1), 65−71.
(20) Burduşel, A. C.; Gherasim, O.; Grumezescu, A. M.; Mogoantă, L.; Ficai, A.; Andronescu, E. Biomedical Applications of Silver Nanoparticles: An up-to-Date Overview. *Nanomaterials* **2018**, *8* (9), 681.
(21) Dutta, D.; Goswami, S.; Dubey, R.; Dwivedi, S. K.; Puzari, A. Antimicrobial Activity of Silver-Coated Hollow Poly-(Methylmethacrylate) Microspheres for Water Decontamination. *Environ. Sci. Eur.* **2021**, *33* (1), 22.
(22) Riau, A. K.; Aung, T. T.; Setiawan, M.; Yang, L.; Yam, G. H. F.; Beuerman, R. W.; Venkatraman, S. S.; Mehta, J. S. Surface Immobilization of Nano-Silver on Polymeric Medical Devices to Prevent Bacterial Biofilm Formation. *Pathogens* **2019**, *8* (3), 93.
(23) Al-Qahtani, M.; Safan, A.; Jassim, G.; Abadla, S. Efficacy of Anti-Microbial Catheters in Preventing Catheter Associated Urinary Tract Infections in Hospitalized Patients: A Review on Recent Updates. *J. Infect. Public Heal.* **2019**, *12* (6), 760−766.
(24) Bondarenko, O.; Ivask, A.; Käkinen, A.; Kurvet, I.; Kahru, A. Particle-Cell Contact Enhances Antibacterial Activity of Silver Nanoparticles. *PLoS One* **2013**, *8* (5), e64060.
(25) Qin, S.; Xu, K.; Nie, B.; Ji, F.; Zhang, H. Approaches Based on Passive and Active Antibacterial Coating on Titanium to Achieve Antibacterial Activity. *J. Biomed. Mater. Res. - Part A* **2018**, *106* (9), 2531−2539.
(26) Wang, X.; Herting, G.; Odnevall Wallinder, I.; Blomberg, E. Adsorption of Bovine Serum Albumin on Silver Surfaces Enhances the Release of Silver at PH Neutral Conditions. *Phys. Chem. Chem. Phys.* **2015**, *17* (28), 18524−18534.
(27) Yuan, Z.; Zhao, Y.; Yang, W.; Hu, Y.; Cai, K.; Liu, P.; Ding, H. Fabrication of Antibacterial Surface via UV-Inducing Dopamine Polymerization Combined with Co-Deposition Ag Nanoparticles. *Mater. Lett.* **2016**, *183*, 85−89.
(28) Xie, Y.; Tang, C.; Wang, Z.; Xu, Y.; Zhao, W.; Sun, S.; Zhao, C. Co-Deposition towards Mussel-Inspired Antifouling and Antibacterial Membranes by Using Zwitterionic Polymers and Silver Nanoparticles. *J. Mater. Chem. B* **2017**, *5* (34), 7186−7193.
(29) Xie, Y.; Chen, S.; Zhang, X.; Shi, Z.; Wei, Z.; Bao, J.; Zhao, W.; Zhao, C. Engineering of Tannic Acid Inspired Antifouling and Antibacterial Membranes through Co-Deposition of Zwitterionic Polymers and Ag Nanoparticles. *Ind. Eng. Chem. Res.* **2019**, *58* (27), 11689−11697.
(30) Bonilla-Gameros, L.; Chevallier, P.; Sarkissian, A.; Mantovani, D. Silver-Based Antibacterial Strategies for Healthcare-Associated Infections: Processes, Challenges, and Regulations. An Integrated Review. *Nanomed. Nanotechnol. Biol. Med.* **2020**, *24*, 102142.

https://doi.org/10.1021/acscentsci.1c01556
ACS Cent. Sci. 2022, 8, 546−561

(31) Panácek, A.; Smékalová, M.; Kilianová, M.; Prucek, R.; Bogdanová, K.; Věcěrová, R.; Kolár, M.; Havrdová, M.; Płaza, G. A.; Chojniak, J.; et al. Strong and Nonspecific Synergistic Antibacterial Efficiency of Antibiotics Combined with Silver Nanoparticles at Very Low Concentrations Showing No Cytotoxic Effect. *Molecules* **2016**, *21* (1), 26.
(32) Tang, S.; Zheng, J. Antibacterial Activity of Silver Nanoparticles: Structural Effects. *Adv. Healthc. Mater.* **2018**, *7* (13), 1701503.
(33) Almeida, L. C.; Frade, T.; Correia, R. D.; Niu, Y.; Jin, G.; Correia, J. P.; Viana, A. S. Electrosynthesis of Polydopamine-Ethanolamine Films for the Development of Immunosensing Interfaces. *Sci. Rep.* **2021**, *11* (1), 2237.
(34) Yang, Z.; Wu, Y.; Wang, J.; Cao, B.; Tang, C. Y. In Situ Reduction of Silver by Polydopamine: A Novel Antimicrobial Modification of a Thin-Film Composite Polyamide Membrane. *Environ. Sci. Technol.* **2016**, *50* (17), 9543−9550.
(35) Mei, Y.; Yu, K.; Lo, J. C. Y.; Takeuchi, L. E.; Hadjesfandiari, N.; Yazdani-Ahmadabadi, H.; Brooks, D. E.; Lange, D.; Kizhakkedathu, J. N. Polymer-Nanoparticle Interaction as a Design Principle in the Development of a Durable Ultrathin Universal Binary Antibiofilm Coating with Long-Term Activity. *ACS Nano* **2018**, *12* (12), 11881−11891.
(36) Wang, J.; Wu, Y.; Yang, Z.; Guo, H.; Cao, B.; Tang, C. Y. A Novel Gravity-Driven Nanofibrous Membrane for Point-of-Use Water Disinfection: Polydopamine-Induced in Situ Silver Incorporation. *Sci. Rep.* **2017**, *7* (1), 3−10.
(37) Bi, C.; Yuan, Y.; Tu, Y.; Wu, J.; Liang, Y.; Li, Y.; He, X.; Chen, L.; Zhang, Y. Facile Synthesis of Hydrophilic Magnetic Graphene Nanocomposites via Dopamine Self-Polymerization and Michael Addition for Selective Enrichment of N-Linked Glycopeptides. *Sci. Rep.* **2020**, *10* (1), 71.
(38) Zhang, Y.; Thingholm, B.; Goldie, K. N.; Ogaki, R.; Städler, B. Assembly of Poly(Dopamine) Films Mixed with a Nonionic Polymer. *Langmuir* **2012**, *28* (51), 17585−17592.
(39) Morgan, S. D.; Rigby, D.; Stickler, D. J. A Study of the Structure of the Crystalline Bacterial Biofilms That Can Encrust and Block Silver Foley Catheters. *Urol. Res.* **2009**, *37* (2), 89−93.
(40) Desai, D. G.; Liao, K. S.; Cevallos, M. E.; Trautner, B. W. Silver or Nitrofurazone Impregnation of Urinary Catheters Has a Minimal Effect on Uropathogen Adherence. *J. Urol.* **2010**, *184* (6), 2565−2571.
(41) Yu, K.; Alzahrani, A.; Khoddami, S.; Ferreira, D.; Scotland, K. B.; Cheng, J. T. J.; Yazdani-Ahmadabadi, H.; Mei, Y.; Gill, A.; Takeuchi, L. E.; et al. Self-Limiting Mussel Inspired Thin Antifouling Coating with Broad-Spectrum Resistance to Biofilm Formation to Prevent Catheter-Associated Infection in Mouse and Porcine Models. *Adv. Healthc. Mater.* **2021**, *10* (6), 2001573.
(42) Smith, J. N.; Thomas, D. G.; Jolley, H.; Kodali, V. K.; Littke, M. H.; Munusamy, P.; Baer, D. R.; Gaffrey, M. J.; Thrall, B. D.; Teeguarden, J. G. All That Is Silver Is Not Toxic: Silver Ion and Particle Kinetics Reveals the Role of Silver Ion Aging and Dosimetry on the Toxicity of Silver Nanoparticles. *Part. Fibre Toxicol.* **2018**, *15* (1), 47.
(43) Cho, Y. M.; Mizuta, Y.; Akagi, J. I.; Toyoda, T.; Sone, M.; Ogawa, K. Size-Dependent Acute Toxicity of Silver Nanoparticles in Mice. *J. Toxicol. Pathol.* **2018**, *31* (1), 73−80.
(44) Huang, B.; Wei, Z. B.; Yang, L. Y.; Pan, K.; Miao, A. J. Combined Toxicity of Silver Nanoparticles with Hematite or Plastic Nanoparticles toward Two Freshwater Algae. *Environ. Sci. Technol.* **2019**, *53* (7), 3871−3879.
(45) Wirth, S. M.; Bertuccio, A. J.; Cao, F.; Lowry, G. V.; Tilton, R. D. Inhibition of Bacterial Surface Colonization by Immobilized Silver Nanoparticles Depends Critically on the Planktonic Bacterial Concentration. *J. Colloid Interface Sci.* **2016**, *467*, 17−27.
(46) Naik, K.; Kowshik, M. The Silver Lining: Towards the Responsible and Limited Usage of Silver. *J. Appl. Microbiol.* **2017**, *123* (5), 1068−1087.
(47) Ramanauskaite, L.; Snitka, V. The Synthesis of Controlled Shape Nanoplasmonic Silver-Silica Structures by Combining Sol-Gel Technique and Direct Silver Reduction. *Nanoscale Res. Lett.* **2015**, *10* (1), 133.
(48) Rasheed, T.; Bilal, M.; Iqbal, H. M. N.; Li, C. Green Biosynthesis of Silver Nanoparticles Using Leaves Extract of Artemisia Vulgaris and Their Potential Biomedical Applications. *Colloids Surf., B* **2017**, *158*, 408−415.
(49) Raza, M. A.; Kanwal, Z.; Rauf, A.; Sabri, A. N.; Riaz, S.; Naseem, S. Size- and Shape-Dependent Antibacterial Studies of Silver Nanoparticles Synthesized by Wet Chemical Routes. *Nanomaterials* **2016**, *6* (4), 74.
(50) Gurunathan, S.; Qasim, M.; Park, C.; Yoo, H.; Choi, D. Y.; Song, H.; Park, C.; Kim, J. H.; Hong, K. Cytotoxicity and Transcriptomic Analysis of Silver Nanoparticles in Mouse Embryonic Fibroblast Cells. *Int. J. Mol. Sci.* **2018**, *19* (11), 3618.
(51) Gliga, A. R.; Skoglund, S.; Odnevall Wallinder, I.; Fadeel, B.; Karlsson, H. L. Size-Dependent Cytotoxicity of Silver Nanoparticles in Human Lung Cells: The Role of Cellular Uptake, Agglomeration and Ag Release. *Part. Fibre Toxicol.* **2014**, *11* (1), 11.
(52) Peña, B.; Owen, G. R.; Dettelbach, K. E.; Berlinguette, C. P. Spin-Coated Epoxy Resin Embedding Technique Enables Facile SEM/FIB Thickness Determination of Porous Metal Oxide Ultra-Thin Films. *J. Microsc.* **2018**, *270* (3), 302−308.
(53) Yu, K.; Lo, J. C. Y.; Yan, M.; Yang, X.; Brooks, D. E.; Hancock, R. E. W.; Lange, D.; Kizhakkedathu, J. N. Anti-Adhesive Antimicrobial Peptide Coating Prevents Catheter Associated Infection in a Mouse Urinary Infection Model. *Biomaterials* **2017**, *116*, 69−81.
(54) Erbil, H. Y.; Cansoy, C. E. Range of Applicability of the Wenzel and Cassie-Baxter Equations for Superhydrophobic Surfaces. *Langmuir* **2009**, *25* (24), 14135−14145.
(55) Ye, W.; Shi, X.; Su, J.; Chen, Y.; Fu, J.; Zhao, X.; Zhou, F.; Wang, C.; Xue, D. One-Step Reduction and Functionalization Protocol to Synthesize Polydopamine Wrapping Ag/Graphene Hybrid for Efficient Oxidation of Hydroquinone to Benzoquinone. *Appl. Catal. B Environ.* **2014**, *160* (1), 400−407.
(56) Li, H.; Jiang, D.; Huang, Z.; He, K.; Zeng, G.; Chen, A.; Yuan, L.; Peng, M.; Huang, T.; Chen, G. Preparation of Silver-Nanoparticle-Loaded Magnetic Biochar/Poly(Dopamine) Composite as Catalyst for Reduction of Organic Dyes. *J. Colloid Interface Sci.* **2019**, *555*, 460−469.
(57) Wang, F.; Han, R.; Liu, G.; Chen, H.; Ren, T.; Yang, H.; Wen, Y. Construction of Polydopamine/Silver Nanoparticles Multilayer Film for Hydrogen Peroxide Detection. *J. Electroanal. Chem.* **2013**, *706*, 102−107.
(58) Ponzio, F.; Payamyar, P.; Schneider, A.; Winterhalter, M.; Bour, J.; Addiego, F.; Krafft, M. P.; Hemmerle, J.; Ball, V. Polydopamine Films from the Forgotten Air/Water Interface. *J. Phys. Chem. Lett.* **2014**, *5* (19), 3436−3440.
(59) Priyam, A.; Nagar, P.; Sharma, A. K.; Kumar, P. Mussel-Inspired Polydopamine-Polyethylenimine Conjugated Nanoparticles as Efficient Gene Delivery Vectors for Mammalian Cells. *Colloids Surf., B* **2018**, *161*, 403−412.
(60) Lv, Y.; Yang, H. C.; Liang, H. Q.; Wan, L. S.; Xu, Z. K. Nanofiltration Membranes via Co-Deposition of Polydopamine/Polyethylenimine Followed by Cross-Linking. *J. Membr. Sci.* **2015**, *476*, 50−58.
(61) Errokh, A.; Magnin, A.; Putaux, J. L.; Boufi, S. Hybrid Nanocellulose Decorated with Silver Nanoparticles as Reinforcing Filler with Antibacterial Properties. *Mater. Sci. Eng., C* **2019**, *105* (July), 110044.
(62) Pandoli, O.; Martins, R. D. S.; Romani, E. C.; Paciornik, S.; Maurício, M. H. D. P.; Alves, H. D. L.; Pereira-Meirelles, F. V.; Luz, E. L.; Koller, S. M. L.; Valiente, H.; et al. Colloidal Silver Nanoparticles: An Effective Nano-Filler Material to Prevent Fungal Proliferation in Bamboo. *RSC Adv.* **2016**, *6* (100), 98325−98336.
(63) Grewal, M. S.; Abe, H.; Matsuo, Y.; Yabu, H. Aqueous Dispersion and Tuning Surface Charges of Polytetrafluoroethylene Particles by Bioinspired Polydopamine-Polyethyleneimine Coating via One-Step Method. *R. Soc. Open Sci.* **2021**, *8* (8), 210582.

https://doi.org/10.1021/acscentsci.1c01556
ACS Cent. Sci. 2022, 8, 546−561